CHAPTER 1. BACKGROUND

1.1 Introduction for Nitride-based materials

The nitrides and nitride-based materials studied in this thesis can be simply divided into two categories: 1) transition metal nitrides, such as TiN, TaN and their alloys; 2) III-nitrides, such as AlN and other related alloys. In these two sections, each of nitride materials will be introduced based on their properties (including structural, mechanical, electrical, thermal, and optical properties), thin film processing, and applications.

1.1.1 Transition-metal-nitrides

Transition-metal nitrides, commonly referred to as refractory hard metals, possess a unusual combination of physical and chemical properties,[1] which make them attractive from both fundamental and technological points of view. They usually have high melting points, extremely high hardness, good electrical and thermal conductivity, and good corrosion resistance. This unique combination of properties has challenged both theoretical and experimental investigations [2-5] of the nature of the chemical bond in these materials and also made possible a large variety of applications[1,6], for example, diffusion barriers in microelectronics, hard wear resistant coatings on cutting tools, and a corrosion and abrasion resistant layers on optical and mechanical components. With the increasingly sophisticated microstructural and compositional design of state-of-the-art nitride films, their performance relies on a corresponding stability. Examples of microstructurally engineered materials include metastable alloy nitrides such as cubic-phase (Ti,Al)N films, Ti(C,N) films in a state of compressive residual stress, and compositionally modulated nitride films (e.g. nanolaminates; multilayers; superlattices).

Generally, transition metal nitrides include TiN, ZrN, VN, NbN, TaN, WN and so on. Their general structural, thermodynamic, mechanical, electrical and magnetic property information are listed in following tables. In this thesis, the main transition metal nitrides studied are TiN and TaN. Their structural, mechanical, and electrical properties are discussed and compared. Their applications for hardcoatings and diffusion barriers are presented.

1.1.1.1 Database of Transition-metal-nitrides

1. Structural database

Formula	Formula Weight	Color	Density $kg/m^3 x10^{-3}$	Crystal structure	Lattice parameters		
					a(nm)	b(nm)	c(nm)
TiN	61.91	Yellow	5.44	Cubic	0.4249	-	-
VN	64.95	Light brown	6.08	Cubic	0.4136	-	-
CrN	66	Black	6.14	Cubic	0.4149	-	-
ZrN	105.23	Light yellow	7.35	Cubic	0.4577	-	-
NbN	106.91	Light gray	8.36	Cubic	0.4392	-	-
Mo_2N	205.89	Dark gray	8.04	Cubic	0.4169	-	-
HfN	192.50	Light brown	13.94	Cubic	0.4392	-	-
TaN	194.96	Gray/blue	14.36	Hexagonal	0.519	-	0.291

Table 1. Formula, formula weight, color, theoretical density, crystal structure and lattice parameters of transition metal nitrides. (Ref. 8)

One point need to be mentioned here is that the data listed here are mainly from the bulk material study, so the numbers may vary from the data of thin films. Even for the data of

thin films, the different deposition techniques and various microstructures may cause variation in these characteristics.

From the above table we find that most of the transition metal nitrides are yellow, brown or gray color, with a face centered cubic structure (sodium chloride structure NaCl). TaN is the only one which has the stable phase of hexagonal structure, while its cubic phase is metastable. The detailed differences between TiN and TaN in structural property properties are discussed in the following sections.

The simple diagram of NaCl structure is shown in figure 1. Among the low index surfaces of the sodium chloride structure, the (100) and (110) surfaces have equal concentrations of metal and nonmetal atoms in each layer at stoichiometric composition. Along the (111) direction, the crystals are composed of alternating layers of metal and nonmetal atoms, giving polar surfaces, which have been found to be metal-terminated. The different crystal structures are the result of different stacking sequences of these layers.

Among the low-index surfaces of the sodium chloride structure the (111) surface has been found to be the most reactive while the (100) surface has been found to be the most inert. Repeated high-temperature annealing cycles, sometimes combined with a short initial sputtering cycle, has been the common method for preparing clean and well ordered surfaces of these materials in situ. For more reactive surfaces, like the (111) and even the (110) of some nitride crystals, this cleaning method has however failed and no investigations of such surfaces have so far been reported. Due to these experimental difficulties, the majority of surface experimental information to date has therefore been collected on (100) surfaces. [7]

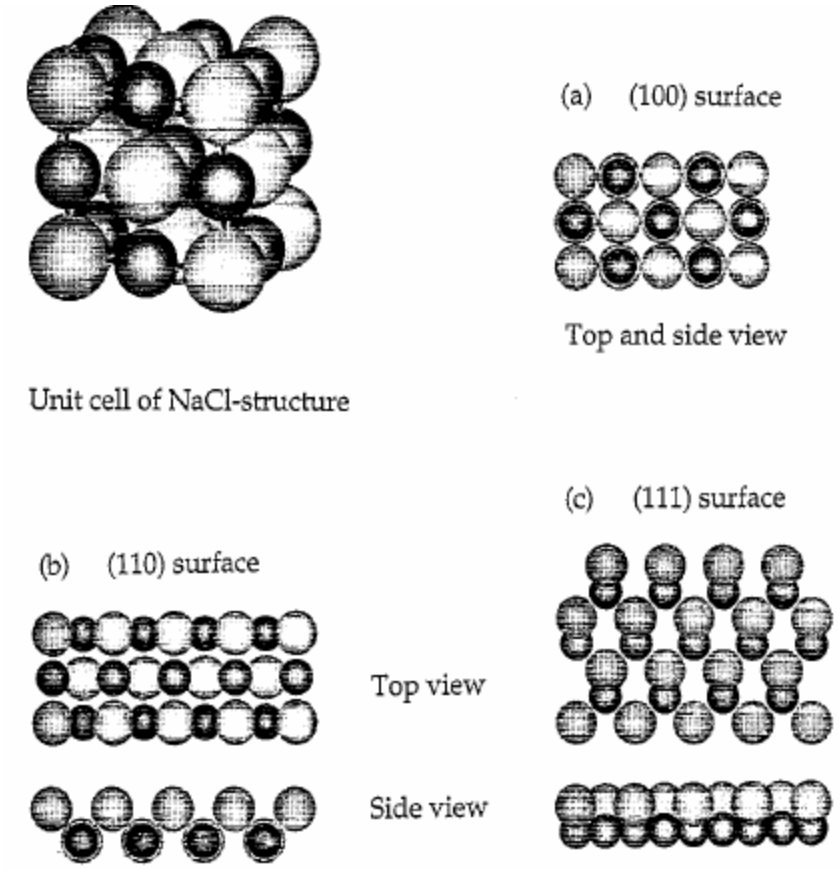

Figure 1. Unit cell of the NaCl crystal structure and the three low-index surfaces: (a) (100), (b) (110) and (c) (111) assuming perfect bulk truncation. The darker spheres present nonmetal atoms and the lighter spheres metal atoms. (Ref. 7)

Those structural and surface characteristics will directly affect the bonding and electrical properties of these transition metal nitrides. We will extensively discuss the bonding and electrical properties of TiN as an example for all the other transition metal nitrides in section 1.1.1.2 and 1.1.1.3.

2. Thermodynamic and thermal property database

Formula	$\Delta_f H^o_{298}$ (kJ/mol)	$\Delta_f G^o_{298}$ (kJ/mol)	S^o_{298} (J/mol•K)	T_{mp} (K)	$\Delta_f H^o_{298}$ (kJ/mol)
TiN	-337.7	-308.9	30.2	3223	66.9
VN	-217.2	-191.1	37.3	2450	-
CrN	-117.2	-92.8	37.7	1773	-
ZrN	-365.3	-337.0	38.9	3225	67.4
NbN	-220.3	-194.8	35.3	2323	46.0
Mo_2N	-	-	-	1173	-
HfN	-373.6	-345.5	44.8	3660	-
TaN	-252.3	-223.9	41.8	3363	67.0

Table.2. Enthalpy of formation, Gibbs free energy formation, entropy, melting point temperature, and heat of fusion. (Ref. 8)

From thermodynamic properties of transition metal nitrides, one can conclude that most of transition metal nitrides listed above have very high melting point and are very stable at room temperature. Especially TiN, ZrN, HfN and TaN, their melting points are around 3000^oC, so they are widely used as high temperature coating and diffusion barrier materials for copper interconnect in IC technology. The detailed hard coating and diffusion barrier applications will be discussed in the following sections.

3. Mechanical property database

Formula	Micro-hardness Hv at load (GPa, N)		Young's Modulus E (GPa)	Poisson's ratio n	Bend Strength s_{bend} (MPa)	Compressive strength s_c (MPa)	Tensile strength s_t (MPa)	Fracture toughness K_{IC} (MPa•$m^{1/2}$)
TiN	19.9	0.5	390	-	260	1298	37	-
VN	13.0±0.5	1	350	-	-	-	-	-
CrN	10.8±0.9	-	320	-	-	-	-	-
ZrN	15.0	1	328	-	190	-	35	-
NbN	18.3±0.5	1	484	-	-	-	28	-
Mo_2N	6.3±0.9	1	-	-	-	-	-	-
HfN	16.7	1	480	-	-	-	-	-
TaN	14.4	1	576	-	-	-	-	-

Table.3 Micro-hardness, Young's Modulus, Poisson's ratio, bend strength, compressive strength, tensile strength and fracture toughness date for transition metal nitrides. (Ref. 8)

Extensive efforts have been directed on mechanical properties of transition metal nitrides. But due to their high hardness and inherent ceramic properties, the mechanical property measurements such as compressive strength and tensile strength measurements have to be performed at elevated temperatures. Mechanical properties of some of these materials have not been reported. But generally speaking, they all have very high

microhardness, and high Young's Modulus and have been widely used as superhard coating materials.

4. Electrical and magnetic property database

Formula	Electrical resistivity r x10^8 (Ω?m)	Temperature coefficient of resistivity		Seeback coefficient, thermal electric power a (μV/K)	Hall coefficient R_Hx10^{10} (m^3/K)	Work function, Φ (eV)	Molar magnetic susceptibility, Xx10^6 (1/mol)
		a x10^3	Range (K)				
TiN	40	0.44	273-1473	-7.7	-0.55	4.09	37
VN	60	0.07	273-1473	-5.0	-1.44	-	130
CrN	640	-	-	-92.0±4.0	-264	-	-
ZrN	18	2.0	77-300	-5.9	-1.44	3.97	22
NbN	54	3.1	77-300	-1.5	0.52	3.92	-
Mo_2N	19.8	-	-	+2.18±0.5	2.83	-	-
HfN	32	1.5	77-300	-2.9	-4.0	4.27	-
TaN	180	0.1	77-300	-1.0	-0.53	-	25

Table 4. Electrical resistivity, temperature coefficient of resistivity, Seeback coefficient, Hall coefficient, work function, and molar magnetic susceptibility. (Ref. 8)

Electrical properties of transition metal nitrides show them to good conductors and possess the electrical characteristics of metals, such as low resistivity, positive temperature coefficient and relatively low work function. The detailed bonding structure and electrical properties of transition metal nitrides is discussed in 1.1.1.2 and 1.1.1.3 using TiN as an example.

One point need to be mentioned here is that the data listed here are mainly from the bulk material study, so the values may vary from that of thin film, as a function of microstructure. Even for the data of the thin films, the different deposition techniques may cause variation in microstructural characteristics. For example, the electrical resistivity of single crystal TiN thin film by pulsed laser deposition was reported to be as low as 15 $m\Omega$cm, which is even smaller than the above listed bulk value. [9] It is reasoned as, the grain boundaries and defects such as dislocations, stacking faults and point defects, including impurities and vacancies in single crystal TiN by PLD are much less than in the bulk-processed TiN. So those grain boundary and defect induced resistivity are relatively lower in epitaxial TiN thin films. One more interesting point here is the electrical properties of TaN. Due to hexagonal structure, TaN is the stable phase, so all the bulk processed TaN specimens have primarily hexagonal structure. The data reported above are all for hexagonal TaN. But recent research on diffusion barrier applications of TaN has shown the metastable cubic phase of TaN become more attractive. So extensive work has been done towards the processing and property study of cubic TaN. The various TaN phases and corresponding properties will be extensively discussed in 1.1.1.2 and 1.1.1.5.

1.1.1.2 Structures of TiN and TaN

TiN

Over last two decades, TiN has been extensively studied due to its successful use in a variety of thin film applications. For example, the high hardness of TiN makes it a particularly useful material for increasing the wear resistance of high speed steel cutting tools, punches, and metal forming tools. In addition the good corrosion and erosion resistance of TiN, its relative inertness, high sublimation temperature and optical and electronic properties have resulted in TiN coatings being considered for use as diffusion barriers in microelectronic devices, cosmetic gold-colored surfaces, and wavelength-selective transparent optical films.

The interesting properties are related to its structure and bonding characteristics (for bonding characteristics see detail in 1.1.1.3). TiN has a cubic NaCl-type crystal structure with a lattice constant (for stoichiometric materials) of 0.4240nm and a vacancy defect structure that is stable over a wide composition range (0.6<N/Ti<1.16). The schematic diagram of its structure is shown in figure 2.

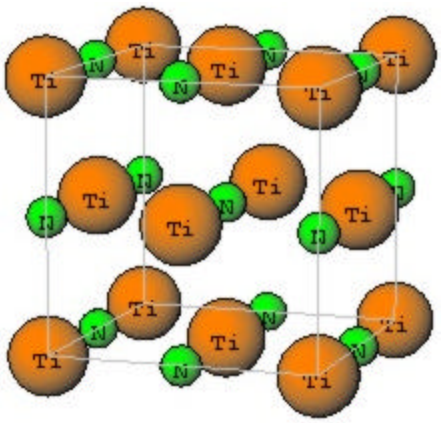

Figure 2. Schematic diagram of crystal structure of TiN (Titanium Nitride) NaCl structure, lattice spacing: a=4.240 angstroms.

TaN

Compared to the phase of TiN thin films, TaN thin films are much more complex, since TaN has different stable phases (such as solid-solution α-Ta(N), hcp-γ-phase, and hexagonal ε-phase) and metastable phases (such as bcc β-TaN, hexagonal δ-phase TaN, hexagonal WC structure θ-TaN and B1 NaCl-structured TaN).[10, 11] Here we will not introduce all 8 phases for TaN, instead of that, all the structure information is listed in table. We will focus on two important phases which form the basis for chapter 4 and 5. One is a stable phase--hexagonal ε-phase TaN, the other one is a metastable phase-- B1 NaCl-structured TaN.

$TaN_{0.05}$	Ta_2N	TaN	δ-TaN	ε-TaN	Ta_5N_6	Ta_4N_5	Ta_3N_5
β phase	γ phase		δ phase	ε phase			
BCC a=0.337nm	HCP a=0.305nm c=0.492nm	FCC a=0.433nm	Hex a=0.293nm c=0.286nm	Hex a=0.518nm c=0.290nm	Hex a=0.293nm c=0.286nm	Tetragonal a=0.683nm c=0.427nm	Tetragonal a=1.022nm c=0.387nm

Table 5. The list of crystallography parameters for all the 8 phases of TaN. (Ref. 10)

For hexagonal ε-phase TaN, the crystallography symmetry is P6/mmm (#191). The schematic diagram in figure shows the structure of ε-phase TaN. (a=0.518nm, c=0.290nm, c/a=0.560)

1 Ta in 1(a): 000

2 Ta in 2 (d): 1/3,2/3,1/2; 2/3,1/3,1/2

3 N in 3 (f): 1/2,0,0; 0,1/2,0; 1/2,1/2,0.

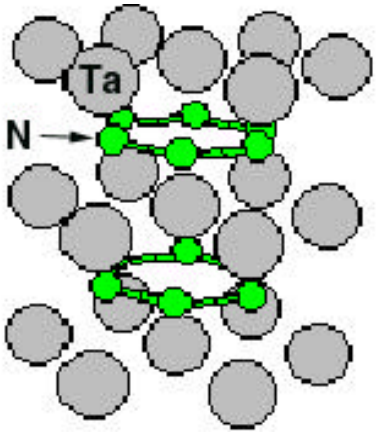

Figure 3. Schematic diagram of structure of ε-phase TaN.

B1 NaCl-structured TaN has the NaCl standard structure which is same as TiN shown in figure and its lattice parameter a=0.433nm.

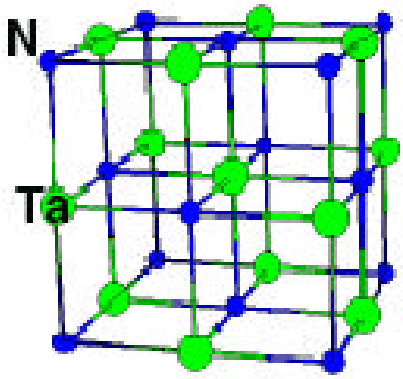

Figure 4. Schematic diagram of structure of B1 NaCl-structured TaN.

TaN hexagonal ε-phase is the stable phase which usually can be obtained by high temperature sintering at 1300^{o}C to 1400^{o}C. So the target for TaN pulsed laser deposition is hexagonal ε-phase TaN determined by X-ray diffraction. But for the applications in diffusion barrier for Cu interconnections, the cubic metastable phase TaN is preferred, due to its structure integrity with Si and its lower resistivity. The detailed diffusion barrier applications for TaN are discussed in section 1.1.1.5.

1.1.1.3 Electrical properties of TiN and TaN

The distribution of charge between the atoms in a solid determines the nature of the chemical bonding. The corresponding electronic states are fundamental importance for the properties of a solid. The electronic states directly involved in the bonding are in an ordered solid described by the band structure, E(k), and are commonly referred to as valence and conduction-band states. The band structure describes the distribution of these states in energy and momentum space and also provides a means for understanding the electronic properties on a microscopic level. In band-structure calculation an infinite crystal having translation symmetry determined by the crystal lattice is assumed and the band structure describes the bulk electron states. However, presence of the surface, or of vacancies, breaks the assumed symmetry and may result in charge rearrangements giving rise to specific surface or vacancy electron states. [2-4]

Electron state involved in the bonding

The band structure calculations of the first and second row of transition metal nitrides can be based on the APW (Augmented Plane Wave) or LAPW (linear APW) methods. [4] But the compounds belonging to the third row such as TaN involves 5d transition metals. So the relativistic effects have to be included in the treatment of the heavier transition metals and the presence of 4f states in the occupied energy region complicates the bonding. So far no literature discussed in detail about the calculation of TaN band structures. Fortunately, TiN band structure has been studied by several groups and band structures of transition-metal-nitrides are fairly similar. Figure 3 shows the band structures of TiN calculated by APW method. It is characterized by an energetically low-lying band, which

is derived from nonmetal 2s states. Separated by an energy gap from the nonmetal 2s band, three overlapping bands are found, which originate from the state G labeled G_{15}. These bands can be derived from the 2p states of nonmetal atom but contain also a significant contribution of states with d-symmetry. The amount of hybridization varies from compound to compound. The next five bands, which originate at G_{25} and G_{12} are predominantly derived from transition metal d-states, but exhibit also some p character. The highest-lying bands represent a mixture of states with different symmetries, originating from both constituents. [12]

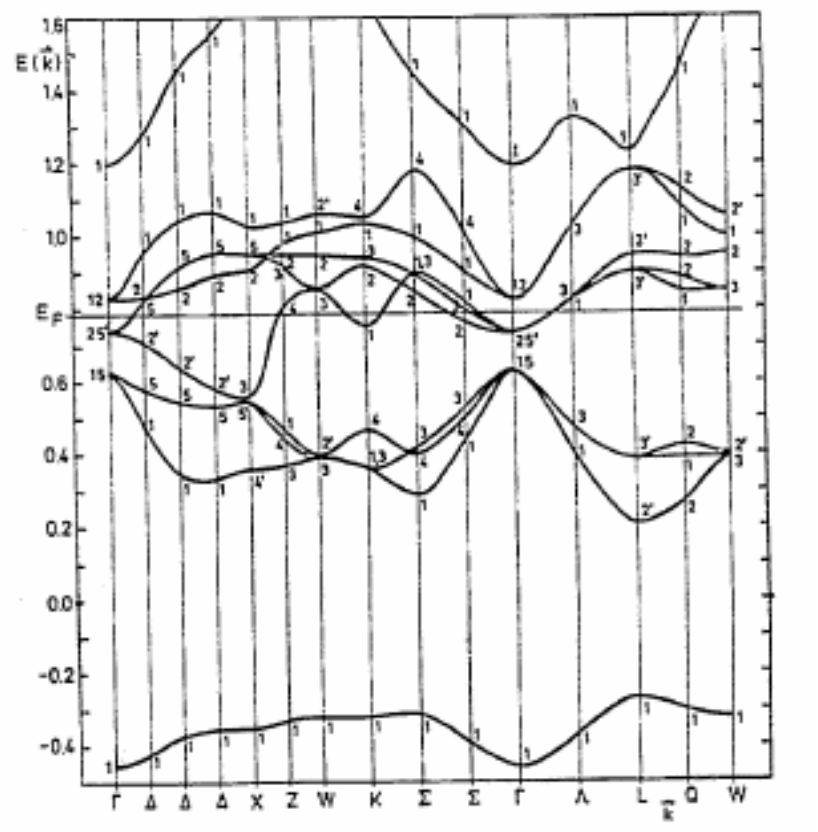

Figure 5. Band structure of TiN calculated using the APW method. (Ref. 12).

Bulk energy band mappings

Detailed information about the band structure in solid can be extracted from angle-resolved photoemission experiments (ARP) on single crystals. [13-16] Location and dispersion of two-dimensional energy bands are usually mapped out by determining the energy positions of features in photoemission spectra. The calculated band structure of TiN along G-X symmetry direction is shown in figure, by solid line. The dotted lines and open dots represent the position of shoulders and peaks in the ARP spectra. This band mapping was derived from non-emission spectra recorded using synchrotron radiation and photon energies from about 15 to 35 eV. Individual bulk bands and their symmetry and dispersions can be identified and mapped out by applying the direct-transition model.[17]

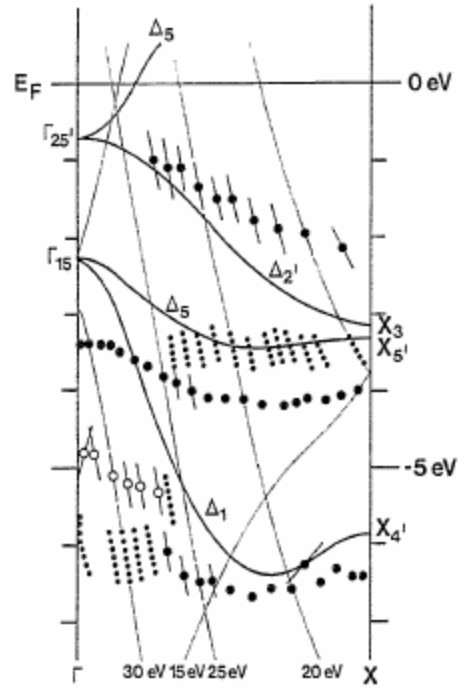

Figure 6. Calculated (solid lines) and experimental (solid dots) bulk energy band dispersions along the <100> direction for TiN. The thin solid lines represent the ?$_1$ final-state bands displaced downwards by the amounts indicated. (Ref. 17).

Core-level electron binding energies are element-specific but experience in molecules and solid chemical shifts that are related to the chemical environment.[18] These shifts can be explained by the redistribution of charge that occurs in the outer electron orbitals when a chemical bond is formed. In a simplified ionic model, a spherical "valence shell" model,[18] the binding energy of a core electron is expected to increase/decrease if charge is removed/add from the valence shell. This is the basic idea which has been exploited in transition metal nitrides to observe the chemical shifts. Band structure calculations show that the bonding contains a significant amount of ionic character and indicate charge transfer from the metal to the nonmetal atoms upon compound formation. The charge transfer from the metal atoms is moreover expected to be largest at stoichiometric composition and to decrease with increasing amount of nonmetal vacancies. In metals and metallic compounds the core-level binding energy is commonly determined relative to the Fermi energy. [19-20]

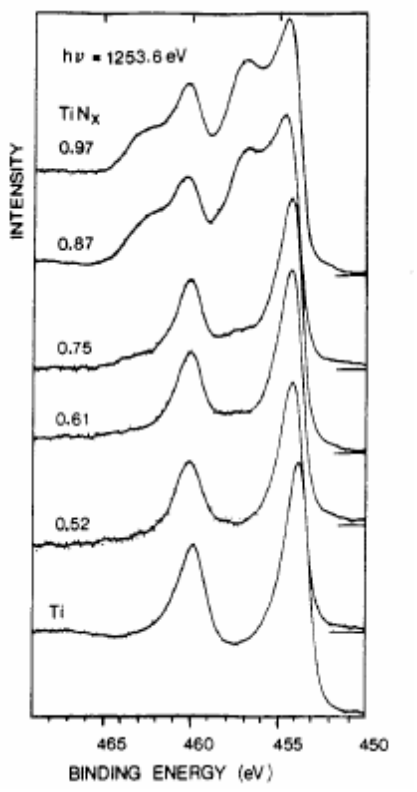

Figure 7.Ti 2p XPS spectra from TiNx and metallic titanium (Ref .21)

Figure 7 shows the core-level shift for different Ti concentration. It is clear that, the energy separation between the metal level and nonmetal level increased with increasing x, indicating a larger charge transfer from metal to nonmetal atoms with increasing x.[21]

1.1.1.4 Mechanical properties of TiN

TiN

The bulk TiN hardness and other mechanical properties are listed in 1.1.1.1 data base. The microhardness value is about 19.9GPa (1990 kg/mm^2). For TiN thin films, the hardness value varies from 3.4 GPa to 40GPa (340-4000 kg/mm^2). The large differences arise primarily from differences in thin film microstructures, such as grain size, columnar vs. equiaxed structure, void density and so on, and film purity. The first microhardness of single crystal TiN thin film was reported by Johansson et al.[22] in 1984 and it is 23±2 GPa (2300±200 kg/mm^2). The sample was grown on MgO substrate and the hardness was measured by Vickers hardness measurement. The reason for lower hardness observed in polycrystalline TiN was explained in the paper to be intergrain boundary failure. They interpret that the dislocation mobility is quite low in most of the transition metal nitrides at temperature below 1000^{o}C.

Johansson et al. also discussed that the polycrystalline films with small grains and dense grain boundaries having sufficient shear strength to force plastic deformation to occur via dislocation movement may actually have somewhat higher hardnesses than single crystals.[22] This is due to the additional component of dislocation scattering from grain boundaries. Similar phenomena were observed in hardness study of nanocrystalline TiN presented in chapter 3. Nanoindentation results show that hardness of single crystal TiN

thin films is 29GPa which is relatively smaller than polycrystalline TiN 32 GPa.(The average grain size is around 100nm.) We envisage this drop to be related to the decrease in overall dislocation density in these single crystal films. If the grain size of TiN thin film continues to decrease in nanocrystalline regime, the hardness is starting to decrease, which is known as negative Hall-Petch relationship.[23] The detailed study of the mechanical property variation of TiN thin film vs. grain size is discussed in chapter 3.

TiN and TiN-based alloy for hard-coating

TiN has been widely used as hard-coating material due to several important characteristics:

(1) High thin film uniformity: TiN coating conforms uniformly to the substrate. No buildup occurs on corners (unlike plating operations) and coating "throws" well into features.

(2) High hardness: Hardness is larger than 2000 kg/mm^2 in Knoop or Vickers Microhardness measurements. Values of 2500-3000 are typical for TiN thin film and it is higher than hard chrome or carbide material.

(3) Good adhesion: The coating forms a metallurgical bond to the substrate that will not flake, blister, chip or peel.

(4) Low coefficient of friction: TiN generally provides relatively low friction against steels, carbides, TiN, ceramics, platings, etc. The coefficient of friction is a system property, not a material property. It depends on many factors such as material, counter-material, lubrication, environment temperature, speed, loading force, surface finish,

surface finish of the counter-material, and type of motion (reciprocating, rotating). The published values have a large variation from 0.50 to 0.90. A typical value is 0.65 for TiN against steel.

(5) Non-stick TiN is an excellent non-stick surface against most other materials.

From above discussions, it is obvious to see the reasons that why the titanium nitride (TiN), has served as the most practical and economical protective coating. TiN exhibits a metallic character with golden color and high hardness, high temperature stability, and abrasion resistance. The golden color can be further adjusted by doping with Zr. However, the TiN gets oxidized above 500^{o}C to form a rutile-structure which limits its applications in high speed cutting tools.[24,25] AlN thin layers have remarkable hardness, thermal and chemical stability and high electrical resistivity. TiN-AlN binary-component coatings can integrate their functionalities and show much higher oxidation resistance, lower internal stresses and better adhesion.[26] TiN-AlN binary-components can be formed in two types of structures. One is uniform alloy which AlN concentration is lower than 60%.[27,28] If AlN concentration is higher than 60%, phase separation results which may lead to precipitation hardening.[29] The other type is mutilayer structure where there is no reaction between TiN and AlN. Especially, nanometer-scale multilayer structures attract a lot of interest due to their special interfacial structure which may lead to novel structural and mechanical properties.[30,31] In chapter 7 we present a novel method to grow highly aligned TiN/AlN superlattice by using pulsed excimer laser. In this method TiN and AlN targets are arranged in a special configuration that they can be ablated in a sequence,

giving alternate layer by layer growth of TiN(1 nm)/AlN(4nm). The structure of AlN is determined to be cubic which is metastable and stabilized by the thin layers of TiN.

1.1.1.5 Diffusion property of TiN and TaN and diffusion barrier applications

1. Diffusion in TiN and TaN

Diffusion measurements in the nitrides are usually difficult to perform due to they have very high melting points and suitable radioactive tracers are often missing. Furthermore, many of these nitride materials are non-stoichiometric and may contain impurities or lattice point defects depending on the variation of PVD process. All of these features can have a large influence on the diffusivity of the metal or nitrogen species in the nitride. The diffusion behavior in nitrides (and carbides) which included the U-N, Pu-N, Si-N, Al-N systems has been reviewed by Matzke in 1992 [32]. The complete collection of diffusion data for carbides, nitrides, hydrides and borides was presented by Matzke and Rondinella in 1999 [33]. Most PVD reactive processes employ low-energy ion irradiation to modify thin film microstructure and composition during growth. However, ion bombardment can also result in potentially detrimental effects such as point defect generation, noble gas incorporation and excess nitrogen composition. Thus, a nitride far from thermodynamic equilibrium will be formed giving rise to different driving forces for diffusion in films. This section considers self-diffusion of N and metals especially Al and Cu in TiN and TaN.

A. Nitrogen diffusion in TiN

Table 7 presents diffusion data for self-diffusion or grain boundary diffusion of nitrogen and impurities in transition metal nitride TiN. N is expected to move by an N vacancy mechanism (octahedral sites), a condition that has been confirmed for TiN [34] and HfN [35]. In general, nitrogen diffuses much faster than the metal atom[32]. An obvious concentration dependence of the diffusion coefficient was found also for the d-$CrN_{1\sim x}$ phase [36] where the N diffusivity decreases with increasing N concentration, while no significant concentration dependence was observed in b-Cr_2 N[36].

System	mechanism	Do (cm^2s^{-1})	Eo (eV)	Temperature(^oC)
N in $TiN_{0.82}$	Self-diffusion	$4x10^{-7}$	2.2	700-1400
N in TiN	Self-diffusion	$5.4x10^{-3}$	2.2	1000-1500
Ar in TiN	Impurity diffusion	1.5x10-14 (Diff. coeff.)	4.43	750

Table 6. Nitrogen and argon diffusion in TiN (Ref. 37)

Low-energy ion assisted deposition of nitride films can lead to oversaturation of nitrogen or inert gas atoms, frequently situated on interstitial sites [38]. Annealing will drive excess N to find empty lattice sites or, as a competing process, precipitate at grain boundaries or as gas bubbles. N_2 precipitation in the form of polyhedral gas bubbles and solid (cubic phase) nitrogen was thus observed in single-crystal TiN films deposited by bias sputtering in pure N_2 discharges at growth temperatures in the range of 500-800^{o}C. For temperatures lower than 500^{o}C, diffusion was too limited during the course of deposition to give rise to precipitation of discernible bubbles whereas for the high-temperature end, segregation and desorption of excess gas at the growing film surface maintained a stoichiometric film composition. [39, 40]

B. Metal Diffusion in TiN

Activation energies for metal diffusion are generally higher for the metal compared to the nitrogen in a given nitride. The metal self-diffusion is via a vacancy mechanism on the metal sublattice [41-44].

Cu and Al diffusion through TiN

The diffusivity of Cu in polycrystalline TiN films by grain boundary diffusion has been measured by several groups including Suni et al.[45] (see Table 2). For example, the diffusion length is 1 nm for annealing at 600°C for 10 min (quartz-tube furnace in flowing Ar 1% H_2). The diffusivity for porous TiN films or films with oxidized grain boundaries is four orders of magnitude higher [45] Grain boundary diffusion of Cu through TiN has an activation energy of 4.43 eV. Al/TiN/Si system has been shown to be stable at annealing temperatures up to 500-600°C for 30 min (quartz-tube furnace in flowing Ar 1% H_2). For low-density TiN films, Si and Al interdiffusion has been reported, presumably along intergranular voids or oxidized grainboundaries. Hultman et al.[46] investigated the thermal stability of Al/dense-polycrystalline-TiN and Al/single-crystal-TiN interfaces and found similar reaction paths and product formation in the two cases. Extensive penetration of Ti into the Al layer, resulting in the formation of a series of Al-Ti intermetalic phases was observed with essentially no diffusion of Al into TiN. Since Ti is the mobile species, which aggressively penetrates Al, newly developed metastable NaCl-structure (Ti, Al) N alloys, provide a much improved barrier behaviour. Petrov et al.[47] thus showed that the extent of interfacial reactions during annealing at 600°C for 150

min was decreased by a factor of 4 by the substitution of $Ti_{0.8}Al_{0.2}N$ barrier layers for TiN.

System	mechanism	Do (cm^2s^{-1})	Eo (eV)	Temperature(^oC)
Ti in TiN/NbN	interdiffusion		2.6	830-875
			4.5	885-930
Cu in TiN	Grain boundary diffusion	$9x10^7$	4.43	608-700
Al in TiN	Grain boundary or surface diffusion	3x10-14	0.3	300-550
Si in TiN	Grain boundary or surface diffusion	$2.5x10^{-14}$	0.3	400-900
Fe in TiN	Grain boundary or surface diffusion	$1.4x10^{-11}$	0.48	200-600
V in AlN		0.3	2.9	1300-1550
Ti in AlN		$4x10^{17}$	8.3	1280-1400
Nb in AlN		13	3.9	400-1600

Table 7. Different metal diffusion in TiN (ref. 37)

Epitaxial growth of TiN films has been reported on various substrates such as Si(001)[48] GaAs(110)[49], and different SiC polytypes[50]. The synthesis of single crystals is also reported for the other nitrides VN, NbN, TaN, ScN, and CrN. The readiness of single-crystal preparation provides for useful model systems in the studies of contacts and diffusion barriers to various crystalline substrates.

For the advanced VLSI technology, the Cu/TaN/Si metalization scheme has recently been introduced commercially. A thin layer of TaN is effective in preventing Cu diffuses into the Si up to at least 600^oC [51]. The barrier failure is usually understood as grain boundary diffusion of Cu through the TaN film. The resistivity of TaN is reported to be relatively

low (150 $m\Omega$cm). For the detail TaN diffusion barrier study, it is discussed in following part of this section. Ta_2N barriers exhibit interfacial reaction with Si substrate, whereas TaN is nonreactive at 700°C[52]. Further improvement in the barrier was reported for Ta-Si-N films which fail by migration of Cu at 900°C [53].

2. TiN diffusion barrier in IC technology

TiN has been widely used in semiconductor *back-ending technology* as a diffusion barrier and interconnect material due to its high stability, low resistivity, good adhesion, and easy processing. *Back-ending technology* refers to the interconnect layers, contacts, vias and dielectric layers that wire the active devices into specific circuit configurations. A schematic diagram showing these components in a typical integrated circuit structure is shown in figure 8. The relative importance of back-end structures has greatly increased in recent years because the circuit delays associate with interconnects have not kept pace with the faster device speeds provided by scaled technologies. Thus much effort has been devoted to improving back-end technology. Interconnects include local and global. Basically, local interconnects are the first, or lowest, level of interconnects. They usually connect gates, sources, and drains in MOS technology, and emitters, bases, and collectors in bipolar technology. In MOS technology a local interconnect, polycrystalline Si, also serve as the gate electrode materials. Silicided gates and silicided sources/drain regions and materials such as TiN and W can also act as local interconnects. Local interconnects can tolerate higher resistivities than global interconnects since they are not very long. And they must be able to withstand higher processing temperatures because they are deposited earlier in the process flow than global interconnects. While for global

interconnects, mostly made of Al right now, are generally all the interconnect levels above the local interconnect level. Because they cover much longer distance, they are always low resistivity metal.[54]

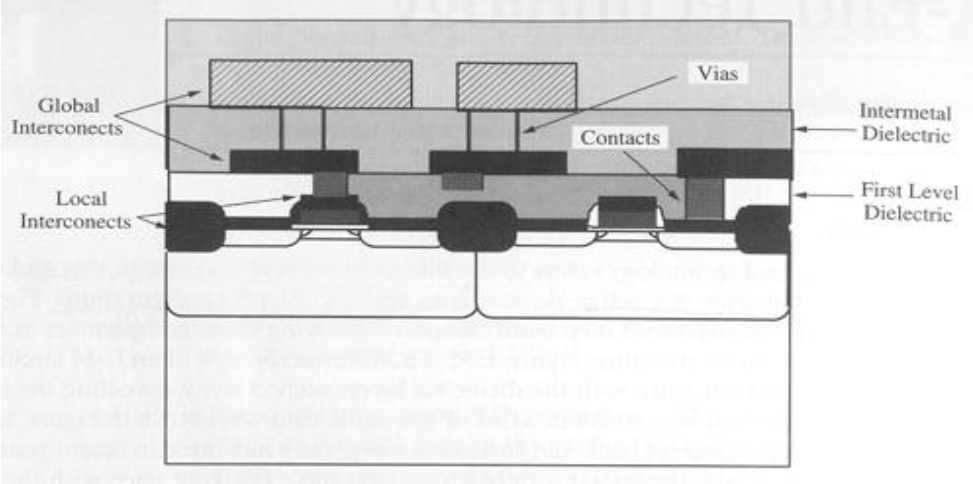

Figure 8. Schematic cross-section of back-end structure, showing interconnects, contacts, and vias, separated by dielectric layers (cross-hatched regions). (Ref. 54)

Al interconnect problems and TiN solution

The main problem for Al interconnect is that thermal stability of Al and significant solubility of Si in Al. 500^{o}C the solubility of Si in Al is about 1 atomic percent. That means that pure Al in contact with Si will attend to absorb the Si from the substrate up to its solubility level at that temperature. And the diffusion of Si in Al is very high, so Al is acting like a sink for Si. Then this will create Si voids in remaining Si, which can be quickly filled by overlaying Al. If Al penetrates uniformly into the substrate, typical processing conditions and contact/interconnect dimensions would result in about 0.2-0.3μm of penetration. However the situation is even worse than that. When Al reduces native oxide, it does so nonuniformly. Al penetrates in localized spots. So Al "spikes"

will occur in Si substrate, penetrating in excess 1 μm. Figure 9 illustrates the formation of Al "spikes" into Si action region.

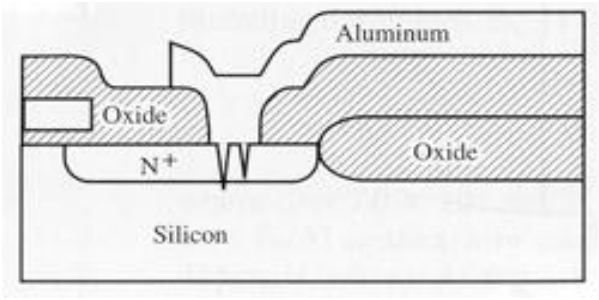

Figure 9. Si-Al contact region showing spiking of Al into Si active region. This is due to Si diffusion into Al to satisfy the solubility requirement, with Al filling the resulting voids in the Si substrate. (Ref. 54)

For this problem, diffusion barrier provides answer. The diffusion barriers need to be a barrier for diffusion between Si and Al at processing temperature (up to 450-500^{o}C). They also need to be thermally stable and low stress. That means the thermal expansion needs to be close to Si (2.6×10^{-6} $^{o}C^{-1}$). They have to adhere well to Si and Al, as well as SiO_2. TiN can be used as a diffusion barrier to alleviate the above problems. TiN thin films are usually fine-grained structures with grain size below 10nm. Diffusion through them is very low and making them impermeable to silicon and most other species. TiN thin films are chemical stable and chemically inert with most other layers. The electrical resistivity of TiN is low enough for use as both a contact material and local interconnect. And TiN is usually used in a bilayer structure with TiN on top of Ti, with Ti usually reacted to form $TiSi_2$ to form better contact. The best properties of these two layers are utilized: the good adhesion and low resistivity of Ti or $TiSi_2$, and the good barrier

property of TiN. This is accomplished without much more processing, since TiN can be easily deposited immediately after Ti, just by adding nitrogen in the sputter deposition chamber. Or TiN can form after annealing Ti in nitrogen.

Another reason for TiN interconnect is to minimize the electromigration of Al. The electromigration is a strong function of the grain texture. The closer all the grains are to a single (111) orientation in vertical direction, the less electromigration occurs. The grain texture of Al is very good on TiN because TiN takes on a pseudogranular structure, continuing the TiN structure to Al interface. Therefore, TiN can reduce the Al electromigration by introducing grain boundaries perpendicular to the current flow. TiN can also be used as a barrier between W and Al layers in semiconductor devices.

3. TaN diffusion barrier in Cu interconnect technology

From Al to Cu interconnects

In order to improve interconnect speed, the delay time t_L has to be kept from increasing too much as the device dimension is scaled down. From this simple equation 1, we can see that if the metal interconnect height H, width W, space Lx, and oxide thickness Xox are smaller, the delay time increases.

$$t_L = 0.89 K_I K_{ox} e_o r L^2 \left(\frac{1}{Hx_{ox}} + \frac{1}{WL_s}\right) \ldots\ldots\ldots\ldots (1)$$

Where, r is the resistivity of interconnect, L, W and H are the interconnect length, width, and height respectively, K_I is added to empirically account for fringing fields and other interconnects above and below the line in multilayer in interconnect systems. K_{ox} and X_{ox} are the oxide dielectric constant and oxide thickness, respectively.

One way to keep the metal thickness H constant is to minimize the reduction in resistivity while shrinking the lateral dimensions. This does slow down the increase in RC delay as the lateral dimensions are scaled. However if the thickness is kept constant, while the lateral dimensions are scaled, the aspect ratios of the features increase making the deposition and etching more difficult. Another option is to actually increase the height, width, and spacing of those interconnects where the major delays occur. These could be the longest lines and would probably be the higher levels of interconnects. Such scheme is commonly used today, with the higher level interconnects kept thicker and wider. But disadvantage of that reverse scaling is fewer metal lines can be fabricated on any level where the line widths and spacing are larger. Other choice could be replacing SiO_2 with lower dielectric constants materials. But the main problems are those materials tend to evaporate or melt when heated and crack easily when subjected to stress.

The most popular trend is replacing Al with lower resistivity materials. Three materials include silver, gold, Copper. Silver has corrosion problems and poor electromigration resistance, and gold has just marginally lower resistivity than Al and contamination problem. Cu has low resistivity, 1.72 $m\Omega$cm versus 2.7 $m\Omega$cm for Al. Additionally, Cu has much better electromigration resistance than Al. Higher electromigration resistance also allows for circuit operation at higher current densities in the interconnects, resulting in potentially faster circuit speed. For these reasons, many manufactures have been developing the new processes that use Cu as interconnect materials.

From TiN to TaN diffusion barrier

The major problem for Cu interconnects is diffusion and contamination of Cu in Si devices. Cu atoms have high diffusivity into underlying dielectric and Si device areas. Diffusion barrier is needed to prevent the diffusion of Cu. Various diffusion barriers are explored, such as TiN, W, Ta, TaSi, W-N, and Ti-W. The base materials of these barriers are refractory metals and the reduction of Cu interdiffusion was achieved by adding a second element such as N or Si. However those materials acting as an effective diffusion barrier, the thickness has to be more than 100nm, which is too thick for the ULSI devices and scaling requirement. The thickness of diffusion barrier has to be scaled down to 10nm to reduce the size and electrical resistivity of barrier/Cu structure.

TaN has become a very promising diffusion barrier material.[55] In previous studies, polycrystalline TaN films have been deposited by a variety of techniques: metal-organic chemical vapor deposition[56], radio-frequency and DC sputtering [57,58] and ionized metal plasma[59]. Since TaN has different stable phases (such as solid-solution α-Ta(N), hcp-γ-phase, and hexagonal ε-phase) and metastable phases (such as bcc β-TaN, hexagonal δ-phase TaN, hexagonal WC structure θ-TaN and B1 NaCl-structured TaN).[60, 61] The structural and electrical properties of polycrystalline TaN films vary a lot with different deposition techniques and different phases. Furthermore, these polycrystalline films tend to grow columnar with grain boundaries normal to the substrate. These grain boundaries of TaN provide faster (pipe) diffusion paths for Cu and reduce its effectiveness as a diffusion barrier. This warrants the deposition of single crystalline TaN films. The single crystalline B1 NaCl-structured TaN film deposition has recently been reported on MgO(100) substrates.[62] However, for microelectronic applications it is desirable to grow

single crystalline TaN on Si. In chapter 4, we report the integration of single crystalline TaN with Si(100) and Si(111) with a buffer layer of TiN, using a pulsed laser deposition, where we explored the lattice-matching epitaxy of TaN and TiN and domain matching epitaxy of TiN on Si.

Diffusion characteristics of Cu in polycrystalline TaN thin films deposited by various techniques have been studied extensively.[63,64] Various techniques have been explored in qualitative and quantitative characterization of Cu diffusion in TaN. For example, sheet resistance study of Cu/TaN/Si were done after various temperature annealing. The results show that TaN can stand up to 800^{o}C annealing without Cu breaking through.[65] SIMS and RBS are the other two depth profiling technique widely used in diffusion study.[66] Results show that TaN can at least stand up to 600^{o}C annealing without Cu diffusing through. But for diffusion depth study and detailed microstructure study of diffusion area, TEM is one of the powerful techniques.[67] But because technically it is very difficult to grow epitaxial cubic-TaN (detail see 1.1.1.6), so far no report on the diffusivity of copper in single crystal cubic NaCl-structured TaN is found in the literature. After we used TiN buffer layer to successfully grow single crystal TaN, the Cu diffusion study in single crystal TaN layer is possible. In Chapter 5 we discuss in detail about the characterization of Cu diffusion in cubic TaN thin films. In order to determine the diffusion characteristics of the single crystalline cubic TaN, we grew a layer of Cu on top of the TaN samples at room temperature and annealed at different temperatures. The diffusivity of Cu into these single crystal cubic TaN films and diffusion activation energy are evaluated and compared with the results of polycrystalline TaN films directly grown on Si by pulsed laser deposition. Both poly and single-crystal films with Cu overlayers were annealed at

500°C, 600°C, 650°C, and 700°C in vacuum to study the copper diffusion characteristics. The diffusion of copper into TaN was studied using STEM-Z contrast, where the contrast is proportional to Z^2 (atomic number), and TEM. The diffusion distances ($2\sqrt{Dt}$) are found to be about 5nm at 650°C for 30 min annealing. The diffusivity of Cu into single crystal TaN follows the relation $D = (160 \pm 9.5)\exp[-(3.27 \pm 0.1)eV / k_B T]cm^2 s^{-1}$ in the temperature range of 600°C to 700°C. We observe that Cu diffusion in polycrystalline TaN thin films is nonuniform with enhanced diffusivities along the grain boundary.

1.1.1.6 Synthesis of TiN and TaN thin film

After we discussed the properties and applications of TiN and TaN, another important issue is the processing of these materials.

TiN deposition

TiN thin films have been deposited by PVD and CVD generally speaking. In PVD, sputtering is commonly used in device fabrications. It is often produced by sputtering a Ti metal target in a nitrogen-containing atmosphere. Sputtering can produce good stoichiometry control and purity control and resistivity of sputtered film is as low as 30-40 $m\Omega$cm.[68] But problem is the conformal coverage. The sputtered diffusion barriers are very thin at the bottom corners of via holes and failure may occur here. Improvements in step coverage of sputtered TiN are achieved by perforated metal masks or ionized metal plasma deposition in current IC production. At the same time extensive exploration of CVD techniques has been carried out over last 15 years. The oldest way is using $TiCl_4$ as

precursor with ammonia and nitrogen as oxidants. The resulting films have good conformality and resistivity is around few hundred $m\Omega$cm. TDMAT and TDEAT are the other precursors used in TiN CVD processing.[69]

These deposition techniques produce conformal films but they are polycrystalline with high values of resistivity. Epitaxial films are expected to reduce film resistivity. First epitaxial TiN growth was reported in 1984 by reactive magnetron sputtering on MgO substrate. [68] The lattice matching and close crystal structure between MgO and TiN facilitated the epitaxial growth. In this paper, Johanson and coworkers also reported the resistivity is as low as 18 μOcm, which proved the single crystal TiN could have much lower resistivity than polycrystalline TiN. The first epitaxial growth of TiN on Si substrate was reported by Narayan et al. at 1992.[70] The large lattice mismatch between TiN and Si lattice was resolved by domain matching epitaxy theory and discussed in detail this thesis in section 1.2. In this thesis, chapter 3 discussed TiN thin film grown by PLD in detail from nanocrystalline to single crystalline. The TEM study of the large lattice mismatch of TiN and Si clearly proved the domain matching epitaxy by observation of ordered misfit dislocation arranged along the interface.

PLD deposited TiN thin films have several advantages. First, good stoichiometry and low impurities. Non-equilibrium processing of PLD can preserve the target concentration into the film concentration. Second, better step coverage because of energetic species. Third, relatively low temperature processing. (see chapter 2.1 PLD for detail information)

TaN depositions

Polycrystalline TaN films have been deposited by a variety of techniques: metal-organic chemical vapor deposition, radio-frequency and DC sputtering, and ionized metal plasma. Most of these deposition efforts are explored in diffusion barrier studies. Since TaN has different stable phases (such as solid-solution α-Ta(N), hcp-γ-phase, and hexagonal ε-phase) and metastable phases (such as bcc β-TaN, hexagonal δ-phase TaN, hexagonal WC structure θ-TaN and B1 NaCl-structured TaN) as we mentioned before, the structural and electrical properties of polycrystalline TaN films vary a lot with different deposition techniques. Furthermore, these polycrystalline films tend to grow columnar with grain boundaries normal to the substrate. These grain boundaries of TaN provide faster (pipe) diffusion paths for Cu and reduce its effectiveness as a diffusion barrier. This warrants the deposition of single crystalline TaN films.

The single crystalline B1 NaCl-structured TaN film deposition has recently been reported on MgO(100) substrates which was deposited by reactive magnetron sputtering. A large amount of efforts was done on CVD growth of single crystalline cubic TaN. For example, TaN by MOCVD using $Ta(NMe_2)_5$ and NH_3 resulted in tetragonal phase Ta_3N_5 with high resistivity (>106mO cm), unsuited to diffusion barrier applications. Recent work has shown that cubic phase low resistivity TaN, suitable for use as a diffusion barrier, can be deposited by MOCVD using the liquid source $(Et_2N)_3Ta{=}N$. It has been proposed that the strong [Ta=N] bond in the molecule leads to the required cubic phase of TaN on pyrolysis.[56] While the $(Et_2N)_3Ta{=}N$ precursor is only available for research applications right now. So far no reports show single crystal cubic TaN thin film processed by CVD.

Further more, for microelectronic applications it is desirable to grow single crystalline TaN on Si. The integration of single crystalline TaN with Si(100) and Si(111) with a buffer layer of TiN, using a pulsed laser deposition was reported in chapter 4 and we can obtain resistivity as low as 220μOcm at room temperature and the diffusion study of Cu proved the cubic TaN thin film can be a very promising diffusion barrier materials for Cu interconnects. Further more, as we added TiN into TaN to form binary components, the resistivity of the structures decreased and the resistivity characteristics changed from semiconductor to metallic behavior. And Cu diffusion in these binary components also shows very promising results (see chapter 6.)

References

1. L. E. Toth, *Transition Metal Carbides and Nitrides*, Academic Press, New York, (1971).
2. J. L. Calais, *Adv. Phys*., **26**, 847(1977).
3. A. Neckel, *Int. J. Quantum Chem*., **23**, 1317(1983).
4. K. Schwarz, *CRC Crit. Rev. Solid State Mater. Sci*. **13**, 11(1987).
5. L. I. Johansson and C. G. Larsson, in Angle Resolved Photoemission, Ed. S. D. Kevan , Springer, Berlin, Ch. 8 (1992).
6. G. Heiners, H. Hantsche, H. A. Jehn, U. Kopacz and A. Rack, *Surf. Coat. Technol*. **55**, 273(1993).
7. L. I. Johansson, *Surface Science Reports* **21**, 177-250(1995).
8. *Carbide, Nitride and Boride Materials Synthesis and Processing*, Ed. by A. W. Weimer, Chapman & Hall, London, 1997.

9. J. Narayan, P. Tiwari, X. Chen, J. Singh, R. Chowdhury and T. Zheleva, Appl. Phys. Lett. **61**, 1290(1992). (J Narayan, U.S. Patent#5, 406,123, April 11,1995)
10. D. Gerstenberg, and C. J. Calbick, J. Appl. Phys. **35**, 402(1964).
11. N. Terao, Jpn. J. Appl. Phys. **10**, 248(1971).
12. A. Neckel, P. Rastl, R. Eibler, P. Weiberger and K. Schwarz, J. Phys. C (Solid State Phys.) **9**, 579 (1976).
13. C. N. Berglund and W. E. Spicer, Phys. Rev. **136**, A1030(1964)
14. B. Feuerbacher and R. F. Willis, J. Phys. C (Solid State Phys.)**9**, 169(1976).
15. N. V. Smith, in Photoemission in Solids I, eds. M. Cardona and L. Ley (Springer, New York, 1978)p. 237.
16. E. W. Plummer and W. Eberhardt, in Advances in Chemistry and Physics, Eds. I. Prigogine and S. A. Rice (Wilet, New York, 1982) P.533.
17. L. I. Johansson, A. Callenas, P. M. Stefan, A. N. Christensen and K. Schwarz, Phy. Rev. B **24**, 1883(1981).
18. K. Siegbahn, C. Nordling, A. Fahlman, R. Nordberg, K. Hamrin, J. Hedman, G. Johansson, T. Berhmark, S. –E. Karlsson, I. Lindgren and B. Lindberg, ESCA, Atomic, Molecular and Solid State Structure Studied by Means of Electron Spectroscopy (Almqvist & Wlksell, Uppsala, 1967).
19. L. Ramqvist, K. Hamrin, G. Johansson, A. Fahlman and C. Nordling, J. Chem. Solids 30, 1835(1969).
20. L. Ramqvist, J. Appl. Phys. 42, 2113(1971).
21. L. Porte, L. Roux and J. Hanus, Phys. Rev. B 28, 3214(1983).

22. B. O. Johansson, J. –E. Sundgren and J. E. Greene J. Vac. Sci. Technol. A 3, 303(1984).
23. C. C. Koch and J. Narayan, Mat. Res. Soc. Symp. **Vol. 634**, B5.1.1(2001).
24. W. Koing, R. Fritsch, D. Kammermeier, , *Surf. Coat. Technol.*, **49**, 316(1991).
25. S. Ikeda, S. Gilles, and B. chenevierf, *Thin Solid Films*, 315, 257(1998).
26. T. Leylendecker, O. Lemmer, S. Esser, and J. Ebberink, *Surf. Coat. Technol*. **48**,175(1991).
27. Y. Tanaka, *J. Vac. Sci. Technol. A* **10**, 1749(1992).
28. T. Ikeda, and H. Satoh, *Thin Solid Films* **195**, 99(1991).
29. O. Knotek, E. Elsing, M. Atzor, and H. G. Prengel, *Wear*, **133,** 189(1989).
30. B. M. Clemens, H. Kung, and S. A. Barnett, *Mater. Res. Soc. Bull.* February, 20 (1999).
31. M. Shinn, and S. A. Barnett, *Appl. Phys. Lett*., **64**, 61(1994).
32. Matzke H. Defect Diffusion Forum 1992;83:111.
33. Matzke Hj, Rondinella VV. In: Diffusion in carbides, nitrides, hydrides, and borides, vol 33, Beke DL, Land-holt,BoKrnstein Numerical Data and Functional Relationships in Science and Technology. Berlin: Springer, 1999 [Chapter 5].
34. Shinozuka K, Susa M, Maruyama T, Nagata K. Defect Diffusion Forum 1997;143}7:1237.
35. Lengauer WJ. Alloys Compounds 1995;229:80.
36. Mayr W, Lengauer W, Ettmayer P, Rafaja D, Bauer J, Bohn M. J Ph Equil 1999;20:35.
37. L. Hultman, Vacuum, **57,** 1-30(2000)

38. Hultman L, Sundgren J-E, Markert LC, Greene JE. J Vac Sci Technol A 1989;7:1187.
39. Wood F, Paasche OG. Thin Solid Films 1977;40:131.
40. Hultman L, Sundgren J-E, Markert LC, Greene JE. J Vac Sci Technol A 1989;7:1187.
41. Holleck H. J Vac Sci Technol A 1986;4:2661.
42. Holleck H, KuKhl C, Schulz H. J Vac Sci Technol A 1985;3:2345.
43. Holleck H, Schultz H. Thin Solid Films 1987;153:11.
44. Matzke Hj. J de Phys C 1979;4:24.
45. Suni I, MaKenpaKaKM, Nicolet M-A, LuomajaKrvi M. J Electrochem Soc 1983;130:1216.
46. Hultman L, Benhenda S, Radnoczi G, Sundgren J-E, Greene JE, Petrov I. Thin Solid Films 1992;215:152.
47. Petrov I, Mojab E, Adibi F, Greene JE, Hultman L, Sundgren JE. J Vac Sci Technol 1993;11:11.
48. Hultman L, Choi C-H, Chiou W-A, Barnett SA. J Vac Sci Technol B 1991;9:221.
49. Zheleva T, Jagannadham K, Narayan J. J Appl Phys 1994;75:860.
50. Hultman L, Ljungcrantz H, Hallin C, JanzeHn E, Sundgren J-E, PeHcz B, Wallenberg LR. J Mater Res 1996;11:2458.
51. Stavrev M, Fischer D, Praessler F, Wenzel C, Drescher K. J Vac Sci Technol A 1999;17:993.
52. Min K-H, Chun K-C, Kim K-B. J Vac Sci Technol B 1996;14:3263.
53. Lee C, Shin Y-H. Mater Chem Phys 1998;57:17.

54. J. D. Plummer, M. Deal, and P. B. Griffin, Silicon VLSI Technology, Fundamentals, Practice and Modeling. Prentice Hall, New Jersey, (2000) P. 681.
55. T. Oku, E. Kawakami, M. Uekubo, K. Takahiro, S. Yamaguchi, M. Murakami, Appl. Surf. Sci. **99**, 265(1996).
56. M. H. Tsai, S. C. Sun, C. P. Lee, H. T. Chiu, C. E. Tsai, S. H. Chuang and S. C. Wu, Thin Solid Films, **270**, 531(1995).
57. H. Mori, J. Imahori, T. Oku and M. Murakami, AIP-Conference-Proceedings, **418**, 475(1998)
58. M. Stavrev, C. Wenzel, A. Moller and K. Drescher, Appl. Sur. Sci., **91**, 257(1995).
59. Y. K. Lee, L. M. khin, J. Kim, and L. Kangsoo, Mater. Sci. in Semiconductor Proc. **3**, 179(2000).
60. D. Gerstenberg, and C. J. Calbick, J. Appl. Phys. **35**, 402(1964).
61. N. Terao, Jpn. J. Appl. Phys. **10**, 248(1971).
62. C. –S. Shin, D. Gall, P. Desjardins, A. Vailionis, H. Kim, I. Petrov, and J. E. Greene, Appl. Phys. Lett. **75**, 3808(1999).
63. T. Oku, E. Kawakami, M. Uekubo, K. Takahiro, S. Yamaguchi, M. Murakami, Appl. Surf. Sci. **99**, 265(1996).
64. M. Stavrev, C. Wenzel, A. Moller and K. Drescher, Appl. Sur. Sci., **91**, 257(1995).
65. Y. K. Lee, K. M. Latt, K. JaeHyung, T. Osipowicz, C. Sher-Yi, and K. Lee, Materials Science and Engineering B77282(2000).

66. M. H. Tsai, S.C. Sun, C. E. Tsai, S. H. Chuang, and H. T. Chiu, J. Appl. Phys. 79, 6932(1996)

1.1.2 III-nitride materials

III-nitride materials have attracted a lot of attention recently, because of potential applications such as blue and ultraviolet light emitting diodes, blue lasers, UV detectors and high-power and high-temperature FETs. Short wavelength light emitters are required for full color display, laser printers, high-density information storage, and underwater communications. High temperature and high power transistors are needed for automobile engines, future advanced power distribution systems. Conventional GaAs based semiconductors are not suitable for designing and fabricating optoelectronic devices in the violet and blue region of the spectrum. These band gaps are not sufficiently large. GaAs based electronic devices cannot be used at high temperatures. III-nitrides are particularly suitable for applications in these areas. The band gaps of III-nitrides are large and direct. The band gap values are 1.9 eV for InN, 3.4 eV for GaN, and 6.2 eV for AlN. Because of their wide band gaps and strong bond strength, they can be used for violet, blue and green light emitting devices and for high temperature transistors. InN and AlN can be alloyed with GaN, this allows tuning of the gaps and emission wavelengths. The nitrides have good thermal conductivity. The III-nitride devices can work not only at much higher temperatures but also in hostile environments. The fact that the nitrides can stand for high temperature makes device-processing easier.[1]

AlN as one of the III-nitride materials, has some outstanding physical properties that have attracted a lot research interests. Its high hardness, high thermal conductivity[2], resistance to high temperature [3] and caustic chemicals,[3] combined with a reasonable thermal match with Si and GaAs, also makes AlN an attractive material for electronic packaging applications.[4] Its wide band gap has led to investigations of its potential as an insulating

material for GaAs and InP based electronic device structures. AlN also has attractive piezoelectric properties[5] and its high sound velocity of 6000m/s[6], which may be suitable for surface acoustic wave device applications. Its thermal stability up to 2000^{o}C and its large nonlinear susceptibility make AlN an outstanding material for nonlinear optics[7]. However, the majority of interest in AlN comes from that it can alloy with GaN which may permit the fabrication of AlGaN based optical devices. These devices are active from the blue wavelengths well into UV.

Another interesting field of research is integration III-nitride LEDs or LDs with Si electronics, these devices will have to grown locally on an already processed Si chip. Therefore considerable work has been done on the growth of III-nitrides on the Si substrate. Thin layers of wurtzite AlN (basal plane lattice parameters, a=0.3112nm) have become widely used as a buffer layer between Si substrate and GaN to improve GaN structural quality and electronic properties. Extensive work has been done on epitaxial growth of AlN on Si(111) substrate and minimizing the dislocation density and other defects.

In this section, properties of AlN will be reviewed in detail from atomic structure to properties such as electrical and optical properties. Corresponding applications will be introduced with its properties. Finally the various crystal growth techniques of AlN on Si(111) and sapphire substrates will be reviewed and compared.

1.1.2.1 Structure of AlN

Stable phase of AlN is wurtzite crystal structure with lattice constant a=0.4982nm, and c=0.3112nm. (P63mc, 186) The schematic diagram of the wurtzite AlN structure is shown in figure 1. AlN also has another two metastable phase-cubic AlN: a=0.412nm (B1, rocksalt) and a=0.433nm (Zincblend). The corresponding properties of wurtzite AlN phase are listed in table 1.

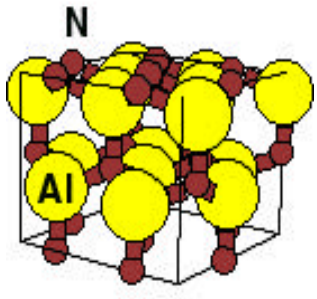

Figure 1. The schematic diagram of the wurtzite AlN structure. (a=0.4982nm, and c=0.3112nm. (P63mc, 186)).

Formula weight	40.99	Band gap energy	Eg(300K)=6.2eV Eg(5K)=6.28eV
Density $kg/m^3 x10^{-3}$	3.26	Index of refraction	n=2.15±0.5
Melting point	3000K	Dielectric constant	e_0=8.5±0.2 e_8 =4.68 e_8 =4.84
Micro hardness GPa	15.3	Phonon modes cm^{-1}	TO=667 E_2=665 LO=910
Young's modulus GPa	400	Thermal expansion 10^{-6}/K	?a/a=4.2 ?c/c=5.3
Electrical conductivity Ω cm	10^{11}	Thermal conductivity W/cm K	K=2

Table 1. The properties of wurtzite AlN phase. (Ref. 3)

1.1.2.3 Electrical properties of AlN

Electrical property characterizations of AlN have been limited to resistivity measurements due to its low intrinsic carrier concentration and deep native defect and impurity energy levels of AlN. Edwards and co-workers [8] observed that transparent AlN single crystals had resistivities ?=10^{11}-$10^{13}\Omega$ cm, a value consistent with other reports. [9] They also found that impure crystals which exhibited a bluish color, possibly due to the presence of Al_2OC, had much lower resistivities ?=10^{3}-$10^{5}\Omega$ cm. These samples were p-type and hall measurements produced a very rough estimate of AlN hole mobility μ_p=14cm^2/Vs. Chu et al. were able to obtain both n- and p- type AlN by introducing Hg, and Se, respectively, however the resistivity of their material was too high to allow the net carrier concentrations to be determined. [10] Rutz et al. observed an interesting transition in AlN films in which resistivity decreased by two orders of magnitude as the applied bias was increased.[11]

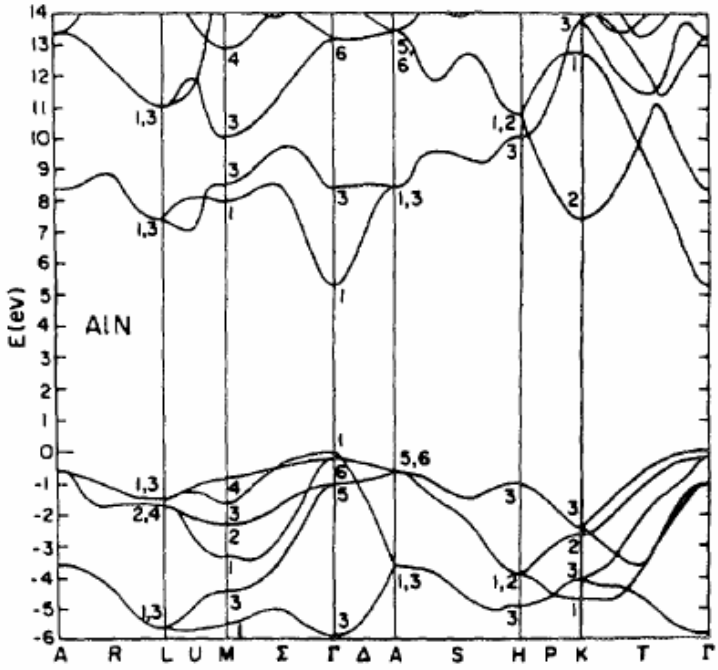

Figure 2. Calculated band structure of wurtzite AlN.(Ref. 14)

Hole effective mass			Electron effective mass		
Top valence band	$m^{//}$	1.5981	Γ_3^c	$\Gamma \rightarrow M(m^{\perp})$	0.3836
				$\Gamma \rightarrow K(m^{\perp})$	0.3836
	$m^{\perp}$	0.2437		$\Gamma \rightarrow A(m^{//})$	4.2211
2nd valence band	$m^{//}$	1.4238	K_2^c	$K \rightarrow \Gamma$	0.7622
				$K \rightarrow M$	0.7682
	$m^{\perp}$	1.4235		$K \rightarrow H$	0.4424
3rd valence band	$m^{//}$	0.2842	M-L	$\Gamma - A$	1.4081
				$K - H$	0.3916
	$m^{\perp}$	1.4235		M	0.4729
				L	0.4729

Table 2. EPM values of the hole effective masses for the top three valence bands of AlN at G, and electron effective masses at relevant secondary minima. (Ref.15)

First calculation of electronic structure of AlN is reported by Hejda using the orthogonalized plane wave method.[12] Bloom [13]and Jones and Lettington[14] used pseudopotential methods to obtain band gaps of 5.25 and 5.31eV, respectively. The calculated band structure is shown in figure 2. Kobayashi et al. reported a band structure of 6.2eV direct band gap calculated using semiconductor empirical tight bonding method. Goano et al. presented the band structure calculation of wurtzite AlN based on nonlocal empirical pseudopotential method employing realistic effective atomic potentials.[15] For each of the constituent atoms in the AlN material, the form of the effective potentials is optimized through an iterative scheme in which the band structures are recursively calculated and selected features are compared to the experimental results. The conduction

band minimum located on the M-L edge of the Brillouin zone is positioning at 0.7542 of M-L segment and energy level at 7.0eV. The calculated values of hole effective masses for the top three valence bands and electron effective masses at relavant secondary minima are listed at Table 2.

1.1.2.2 Optical properties of AlN

The optical properties of AlN such as room temperature band gap, index of refraction, long wavelength dielectric constant and photon modes are listed in Table 1. Yim et al. characterized high-quality AlN by optical absorption and determined the room temperature band gap to be direct with a value of 6.2 eV.[16] Some other measurements of AlN band gap gave much lower value which is probably due to the oxygen contamination.[17] The room temperature absorption spectra of AlN films is shown in figure 3.

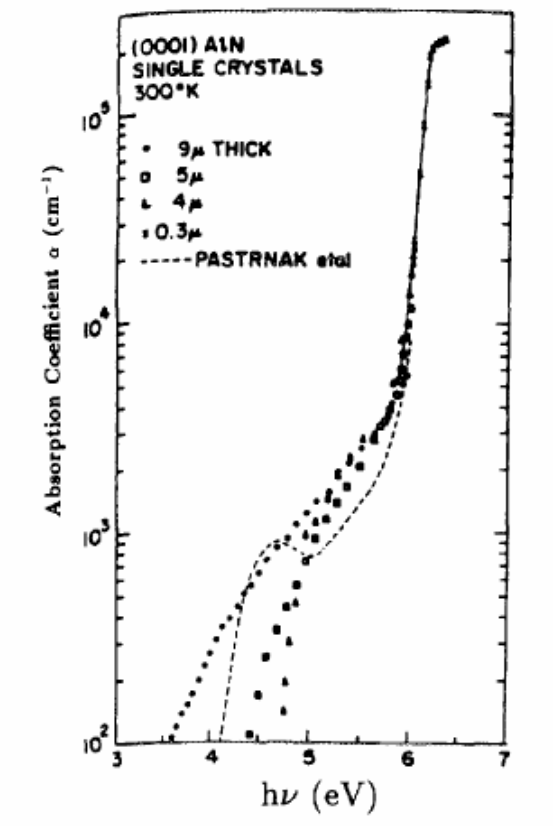

Figure 3. Room-temperature absorption spectra of AlN films of varying thickness whose principle absorption edge occurs at 6.2eV. The bump near 4.5-4.8eV in the data of Pastrnak et al. was attributed to oxygen absorption bands. (Ref. 16)

1.1.2.4 Processing of AlN on sapphire and Si(111)

As we mentioned before, due to AlN has high hardness, high thermal conductivity, resistance to high temperature and caustic chemicals, it is of considerable interest for high-power, high-temperature, and radiation-resistant electric and optoelectronic applications. High quality epitaxial heterostructures are required to fully realize these applications of AlN, because many of these applications are related to crystal structure of the films, epitaxial relations and orientation with the substrate. Especially the electric properties are sensitive to the nature of epitaxial growth and the density of structural defects such as dislocations, twins, and stacking faults, grain boundaries and related defects. While the epitaxial growth characteristics and nature of defects are determined by the thin film growth conditions and substrate variables including temperature, lattice misfit, and interfacial chemical free energy.

Various deposition techniques are explored in the AlN single crystal growth, such as chemical vapor deposition, plasma assisted CVD,[18] metalorganic CVD,[19] reactive dc-magnetron sputtering,[20] plasma assistant molecular beam epitaxy[21], and pulsed laser deposition.[22] Various deposition techniques and related deposition parameters of epitaxial AlN are listed in table 3.

Deposition techniques	**Deposition temperature**	**Pre-deposit materials**	**Substrate**	**Back pressure**	**Other parameters**
CVD	1000^{o}C	AlCl+NH_3	a-Al_2O_3 SiC ZnO	130Pa	
plasma assisted CVD	1000^{o}C	AlCl+NH_3	a-Al_2O_3 SiC ZnO		
Metal organic CVD	1050^{o}C	TMAl	a-Al_2O_3 SiC ZnO	130-300Torr	
reactive dc-magnetron sputtering	650-800^{o}C	Al	a-Al_2O_3 SiC ZnO Si	Ar/N_2 (30/70) 10mTorr	
plasma assistant molecular beam epitaxy	850^{o}C-1150^{o}C	Al+ activated nitrogen	a-Al_2O_3 SiC ZnO	$2x10^{-5}$ Torr N_2	RHEED
pulsed laser deposition	750^{o}C	AlN	a-Al_2O_3 SiC ZnO Si	$5x10^{-5}$ Torr N_2	
Laser-MBE	750^{o}C	AlN	a-Al_2O_3 SiC ZnO Si	$1x10^{-8}$	RHEED

Table 3. List of various deposition techniques and deposition parameters for AlN growth.

Substrate or film for AlN	**Symmetry**	**Lattice parameters(A)**	**Mismatch with AlN (Wurtzite)**
a-Al_2O_3	Hex	a=4.758 c=12.991	13%
6H-SiC	Hex	a=3.08 c=15.12	1%
ZnO	Hex	a=3.252 c=5.313	1%
Si(111)	Diamond	a=5.43	19%
GaN	Hex	a=3.189 c=5.185	2.4%

Table 4. List of various substrates and films for AlN and their lattice mismatch.

AlN on sapphire

Various substrates for AlN growth and lattice misfit are listed in table 4. From the lattice misfit comparison, we can see the prospective substrates for AlN growth are 6H-SiC and a-Al_2O_3. But 6H-SiC substrates are very expensive. More practical substrate is a-Al_2O_3. Extensive work has been done on the epitaxial growth of AlN on a-Al_2O_3 and their orientation relationships. The epitaxial relationship for (0001) sapphire was found to be (0001) AlN // (0001)sapphire, with in plane orientation relationships of $[01\bar{1}0]$AlN // $[2\bar{1}\bar{1}0]$ sapphire and $[2\bar{1}\bar{1}0]$ AlN // $[\bar{1}100]$sapphire. This is equivalent to a 30^o

rotation in the basal (0001) plane. The schematic orientation relationship between AlN and sapphire is shown in figure 4 and figure 5. (Ref.19)

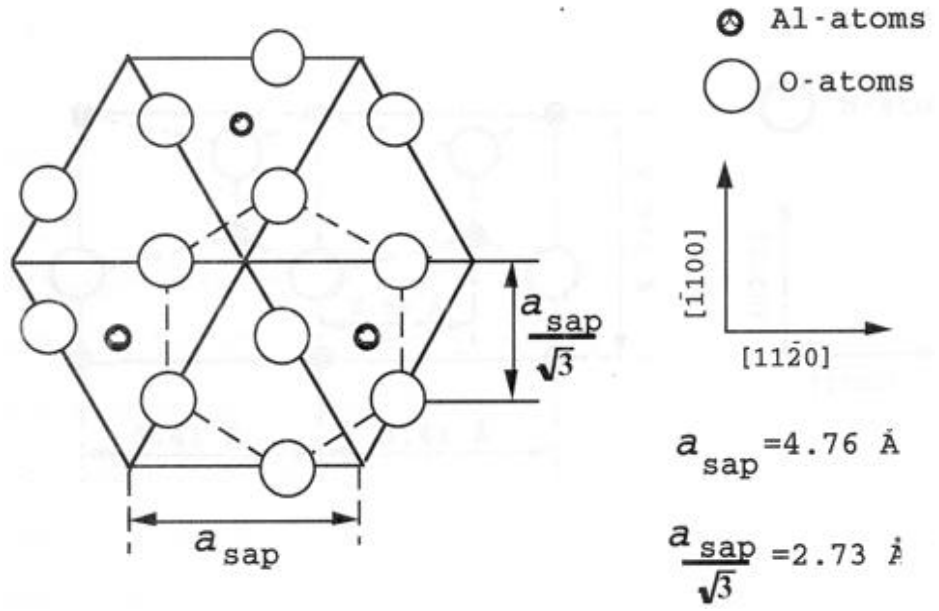

Figure 4. Schematic drawing of (0001) oxygen atoms plane of sapphire (large circle) and positions of Aluminum atoms just above and under this plane (small circles). (Ref.19)

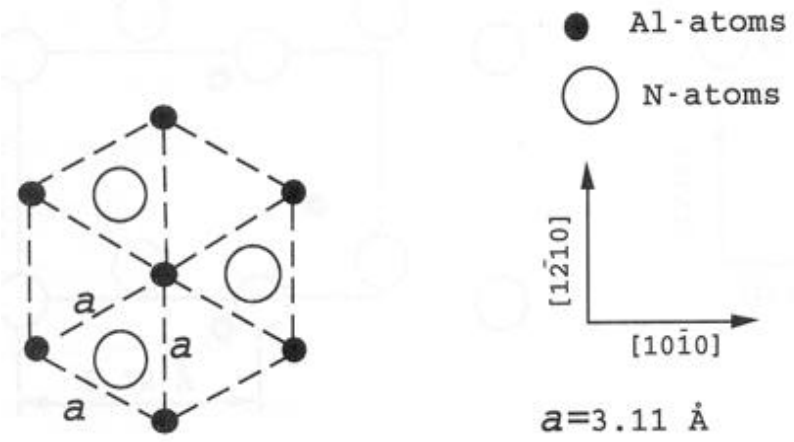

Figure 5. The (0001) plane of AlN; Aluminum and nitrogen atoms belonging to the same plane are indicated by small and large circles correspondingly. (Ref. 19)

While the high lattice misfit between AlN and a-Al_2O_3 make the formation of defects such as threading dislocations. So post deposition annealing becomes a very practical way to anneal the defects away. Some annealing studies have been carried out on MBE grown AlN on SiC samples at 1200-1400^oC. [23] Results showed that the quality of thin films improved markedly and the dislocation density reduced to $3x10^8/cm^2$. But for the annealing effects of AlN on sapphire substrate and the mechanism for dislocation reductions, a lot of research work still need to be carried out.

In my research, the epitaxial AlN was grown on sapphire substrate by pulsed laser deposition and annealed in N_2 pressure at 1300^oC for 30min. The annealing effects such as dislocation density and optical properties were studied. Weak beam condition in TEM was used to study the dislocation density and compare dislocation content between before and after annealing. The transmission measurement was used for optical property characterization. The dislocation density decrease dramatically and transmission improved after annealing, which showed the quality of AlN film improved. The possible mechanisms are discussed in chapter 8.

AlN on Si(111)

As we discussed earlier, the integration III-nitride LEDs or LDs with Si electronics requires III-nitrides thin films grown locally on an already processed Si chip. Thin layers of wurtzite AlN (basal plane lattice parameters, a=0.3112nm) have become widely used as a buffer layer between Si substrate and GaN to improve GaN structural quality and electronic properties. Extensive work has been done on epitaxial growth of AlN on Si(111) substrate and minimizing the dislocation density and other defects. [21, 22, 24]

Epitaxial growth of AlN on Si(111) was reported by Vispute et al.[22] via pulsed laser deposition, Bourret et al. used plasma assisted gas source molecular epitxay, and Kaiser et al. via Plasma-assisted molecular beam epitaxy (MBE). The epitaxial relation between AlN and Si is revealed to be AlN $[2\bar{1}\bar{1}0]$// Si[110] and AlN $[01\bar{1}0]$ // Si[422]. While the large misfit between the spacing of $\{2\bar{1}\bar{1}0\}$AlN planes (a/2=1.556A) and{220} planes of silicon results in 19% strain. Domain matching epitaxy is proposed to resolve this big lattice misfit. But detailed domain relation and experimental proof of the domain matching between AlN and Si has not been reported yet. In order to study this domain matching epitaxy mechanism in AlN on Si(111), epitaxial wurtzite AlN thin films were deposited on Si (111) by laser-molecular-beam-epitaxy. Selected-area diffraction in transmission electron microscope revealed the epitaxial growth of AlN on Si(111) substrate. The orientation-relationship of AlN/Si(111) was studied from Si <110> and <112> zone axes and compared with simulated results. The interface structure and growth mechanism were studied by high-resolution transmission electron microscopy, and Fourier filtered image of cross-sectional AlN/Si(111) samples from both Si <110> and <112> zone axes revealed the domain matching epitaxy of 4:5 ratio between the interplanar distances of Si (110) and AlN $(2\bar{1}\bar{1}0)$. (see chapter 9)

Reference:

1. S. C. Jain, M. Willander, J. Narayan, and R. van. Overstraeten, J. Appl. Phys., **87**, 965(2000).
2. L.M. Sheppard: Am. Ceram. Soc. Bull. **6**9, 1801 (1990)
3. S. Strite, H. Morkoc: J. Vac. Sci. Technol. B **1**0, 1237 (1992)
4. E. S. Dettmer, B. M. Romenesko, H. K. Charles Jr., B. G. Carkhuff, and D. J. Merrill, IEEE Trans. Compoments, Hybrids, Manuf. Technol. 12, 543(1989).
5. A.D. Bykhovski, V.V. Kaminski, M.S. Shur, Q.C. Chen, M.A. Khan: Appl. Phys. Lett. **6**8, 818 (1996)
6. M.T. Duffy, C.C. Wang, D.G. O'Clock Jr., S.H. MacFarlance III, P. Zanzucchi: J. Electron. Mater. 2, 359 (1973)
7. G.T. Kiehne, G.K.L. Wong, J.B. Ketterson: J. Appl. Phys. **8**4, 5922 (1998).
8. K. Kawwabe, R. H. Tredgold, and Y. Inuishi, Elect. Eng. Jpn. **87**, 62(1967).
9. G. A. Cox, D. O. Cummins, K. Kawabe, and R. H. Tredgold, J. Phys. Chem. Solids **28**, 543(1967).
10. T. L. Chu, D. W. Ing, and A. J. Noreika, Solid State Electron, 10, 1023(1967).
11. R. F. Rutz, Appl. Phys. Lett. **28**, 379(1976).
12. B. Hejda, Phys. Status Solidi **32**, 407(1969).
13. S. Bloom, J. Phys. Chem. Solids, **32**, 2027(1971).
14. D. Jones and A. H. Lettington, Solid State Commun. **11**, 701(1972).
15. M. Goano, E. Bellotti, E. Ghillino, G. Ghione, and K. F. Brennan, J. Appl. Phys. **88**, 6467(2000).

16. W. M. Yim, E. J. Stofko, P. J. Zanzucchi, J. I. Pankove, M. Ettenberg, and S. L. Gilbert, J. Appl. Phys. **44**, 292(1973).
17. K. Kawabe, R. H. Tredgold, and Y. Inuishi, Elect. Eng. Jpn, **87,** 62(1967).
18. W. Zhang, Y. Someno, M. Sasaki, and T. Hirai, J. Cryst. Growth **130**, 308(1993).
19. K. Dovidneko, S. Oktyabrsky, J. Narayan, and M. razeghi, J. Appl. Phys. **79**, 2439(1995).
20. W. J. Meng, J. Heremans, and Y. T. Cheng, Appl. Phys. Lett. **59**, 2097(1991).
21. U. Kaiser, P. D. Brown, I. Khodos, D. J. Humphreys, H. P. D. Schenk, and W. Richter, J. Mater. Res, **14**, 2036(1999).
22. R. D. Vispute, J. Narayan, H. Wu, and K. Jagnnadham, J. Appl. Phys. **77**, 4724(1995).
23. Z. Y. Fan, G. Rong, N. Newman, and David J. Smith, Appl. Phys. Lett., **76**, 1839(2000).
24. A. Bourret, A. Barski, J. L. Rouviere, G. Renaud, and A. Barbier, J. Appl. Phys. **83**, 2003(1998).

1.2 Mechanism of epitaxial growth

To realize a full potential of a new technology, epitaxial growth of thin film often present a major bottleneck. Materials such as $Ta_xTi_{1-x}N$, $Ga_xIn_{1-x}N$, $Al_xGa_{1-x}N$, $Zn_xMg_{1-x}O$, $Ba_{0.5}Sr_{0.5}TiO_3$, $La_{0.7}Ca_{0.3}MnO_3$, etc., and their heterostructures are important for diffusion barrier (electrical property), Light Emitting Diodes (LED, optical applications), magnetic field sensors and computer read heads (ferromagnetic properties). The crystal structures that are present in the natural semiconductors are the lowest energy configurations of the solid state of atoms. Since the electronic, optical and magnetic properties of the semiconductor materials are determined by their crystal structure, the fabrication of artificial structures or superlattices, which are metastable phases, is of great interest. The key to grow epitaxial artificial structures with controllable optical and electronic properties is the major challenge for a new device or technology.

1.2.1 Epitaxy Theory and Lattice Matching Epitaxy

Epitaxy is a term used to describe an extended single-crystal film formation on top of a crystalline substrate.[1-4] While *homoepitaxy* refers to the film formation on top of the same material, *heteroepitaxy* refers to the films grown on substrates composed of a different material. When the epilayer and the substrate materials are identical or have same or almost-same lattice constants, there are no strained interfacial bonds, because lattice parameters match perfectly. Such structures are called *lattice-matched epitaxial* heterstructures, as shown in figure 1a. The deposition of epilayer atoms onto the substrate surface allows them to easily locate the potential minima corresponding to the substrate lattice sites, presuming that the adatoms have sufficient energy (i. e. growth temperature

is high enough) to move to the nearest energy minimum. Usually in heteroepitaxial structures, the lattice parameters are different, and hence depending on the mismatch, the film can grow onto the substrate either coherently, called *coherently strained lattice – mismatched heterosepitaxy* (or strained-layer epitaxy) as shown in figure 1b or incoherently called *relaxed lattice mismatched heteroepitaxy* as shown in figure 1c.

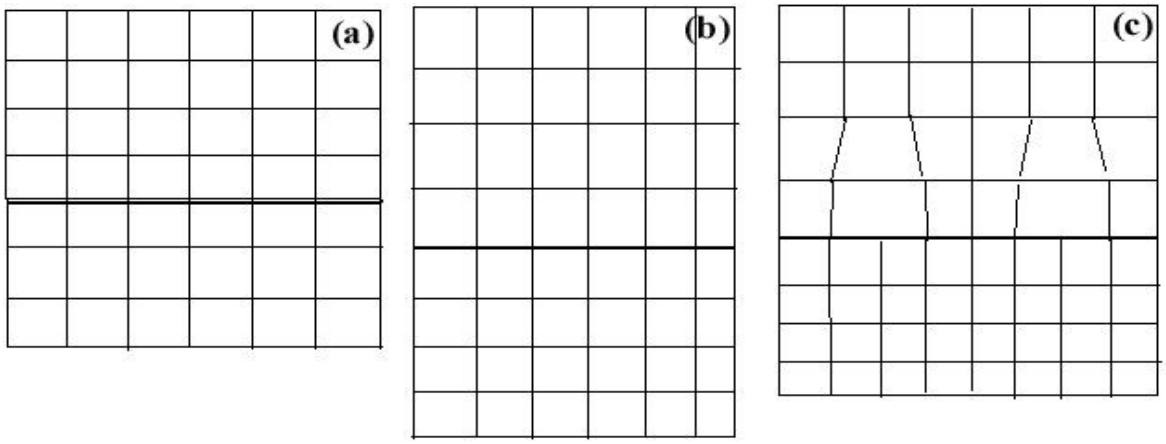

Figure 1. Schematic illustration of (a) lattice matched heteroepitaxy; (b)coherently strained lattice-matched heteroepitaxy; (c) relaxed lattice-mismatched heteroepitaxy.

In the strained layer epitaxy, atoms in the film are constrained to the substrate inter-atomic spacing in the plane of interface despite the difference in the film and substrate lattice parameters. Thus significant elastic strain energy is stored in the structure. For example, accommodation of a lattice mismatch of only 1% in a coherent strained film, produces a stress field about 2 GPa (at shear modulus 5 x 10^{10} Pa, and Poison ratio 0.33) [2]. For a given lattice mismatch the elastic strain energy in the initially coherent film increases linearly with the film thickness. When the strain energy is sufficiently large, at a "critical thickness", the strain at the interface is relieved via the formation of misfit

dislocations and this is called relaxed lattice mismatch mechanism of epitaxy. In heterostructures with a very large lattice mismatch (>10%) such as, TiN on Si with lattice misfit 24.6%, the strain in the film is so large at the very initial stages that the film can not grow coherently from the beginning. In such case the epitaxial growth is achieved via formation of domains when $na_f = (n \pm 1)a_s$, where the a_f and a_s are the film and the substrate lattice parameters, respectively, and n is an integer.[5] The coherency between the film and the substrate is preserved within the domain, while there is a cross-grid of misfit dislocations separating the domains. The mechanism of domain epitaxial growth in very-high-mismatched systems is discussed in detail in section 1.2.2.

Growth Morphology:

In practice epitaxy builds up according to one of the three distinct "growth modes",[6, 7] as shown in figure 2: (a) layer-by-layer, or Frank-van der Merve two-dimensional growth mode (FM); (b) nucleation of three-dimensional clusters (islands) on the plane surface of a substrate, or Volmer-Weber three dimensional growth mode; and (c) formation of three-dimensional clusters (islands) on two-dimensional thin uniform layer, or Stranski-Krastanov growth mode. Bauer[8] has demonstrated that relative surface energies play an important role in determining which growth mode occurs at the thermodynamic equilibrium. If the deposited material has larger surface energy than the substrate, the three-dimensional or island structure is favored; otherwise the film tends to grow in layer-by-layer mode. Recent studies based on continuum elasticity approach predict that layer-by-layer growth is never the equilibrium morphology, but rather it is a metastable with respect to island formation. Three dimensional islands form when the epilayer-

epilayer interactions are much stronger than epilayer-substrate interactions. Experimental studies support these considerations for systems with known surface energy values.

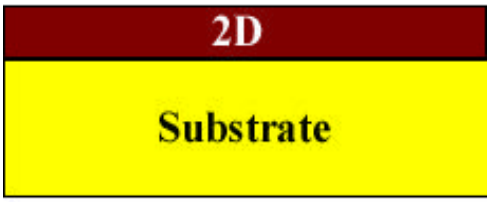

Figure 2. Modes of growth of an overlayer on a substrate:

a) layer-by-layer 2D(Frank-van der Merve);

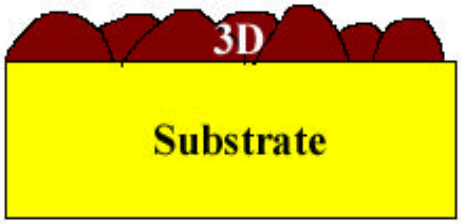

b) island growth 3D (Volmer-Weber);

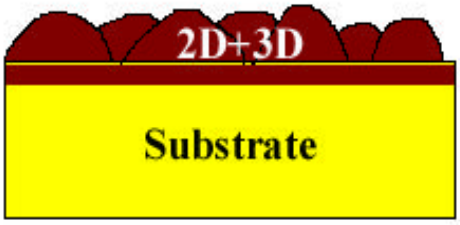

c) island growth on a thin layer 2D and 3D (Stranski-Krastanov).

Stability and relaxation of strained epilayers: As it was stated earlier, beyond a "critical thickness" h_c the coherently strained film relaxes via generation of misfit dislocations. The critical thickness of epilayer is related to the balance between the relief of the coherent strain energy and the extra energy associated with the lattice distortions produced by misfit dislocations. Different theories apply different approaches for critical thickness determination.

Earliest models by Frank and van der Merve [9, 10] showed that : (1) if the misfit f does not exceed critical value of strain e_c, a thin overlayer will grow coherently with the substrate;

(2) even if the strain in the overlayer $|e|\rangle e_c$, the overlayer will be strained with the substrate except that a periodic array of localized regions called misfit dislocations will form; and (3) with the increase of the film thickness the film accumulates elastic strain energy so that above the critical thickness, misfit dislocations form to relieve the strain. Thus, according to van der Merve's criterion, critical thickness is the thickness at which the energy of the coherently strained state becomes equal to the energy of the fully relaxed state.

Matthews and Blakeslee criterion [11,12] is based on the energy minimum condition $dE(hc,n)/dn = 0$ at $n \to 0$, where E is the total energy of the structure and it is a function of the thickness of the film h and the dislocation density n. Ichimura and Narayan pointed out that the difference between the two criteria can be very large.[13]

In addition to the critical thickness as the main issue in misfit strain accommodation process, the mechanisms involving generation of dislocations, including their nature, nucleation, motion and interactions is of increased scientific and applied interest.[14-17] The mechanisms which control dislocation generation are different in low and large lattice mismatch systems. In systems with low mismatch (<2%), the generation of dislocation is nucleation limited because of the high energy barrier for nucleation. The misfit is accommodated first by formation of 60^o dislocations from the surface, which glide half-loops to the interface, and eventually recombine at the interface to form 90^o misfit dislocation. In high-mismatch systems (>2%), the energy barrier for nucleation is low and hence the generation of dislocation is a glide limited process.

Atomic Structure The interest in the atomic structure of defects, and in particular of dislocations in semiconductors, is driven by the fact that defects influence the properties of electronic devices. The positions of atoms in a core region of a dislocation determine the electron distribution and hence their electronic properties. Also, the atomic structure and energetic of dislocations can be used to predict reactions and growth directions of dislocations. In the atomistic modeling, the atomic structures of dislocations are obtained by minimizing the bond distortions and the number of dangling bonds, using energy minimization procedures,[18] which include: (1) choice of atomic cell with appropriate size and boundary conditions; (2) choice of an appropriate potential to calculate the energy of the cell; and (3) minimization of the cell energy by moving every atom sequentially in the direction of force calculated by interatomic potentials.

Thus, understanding the principle mechanisms which control epitaxy on atomic level, the experimental characterization and control of epitaxial growth, and the ability to monitor the chemical and structural properties of the surfaces and heterostructures allows metastable phases and strained-layer heterostructures to be grown. Superlattices introduce new periodicities which determine the electronic structure of subbands originating from the superlattice potential. This subband structures determine the transport, optical, magnetic and other properties of materials.

1.2.2 Domain Matching Epitaxy

The theory of Domain Matching Epitaxy involves matching of lattice planes between the film and the substrate having similar crystal symmetry. In this theory, the conventional lattice matching epitaxy (LME) becomes a special case where a matching of lattice constants or the same planes is involved with a small misfit of less than 7-8%. In large lattice mismatch systems, epitaxial growth of thin films is possible by matching of domains where integral multiples of major lattice planes match across the interface. As we discussed in section 1.2.1, we can easily draw the relation of domain matching epitaxy and traditional lattice matching epitaxy in table 1.

In the domain matching epitaxy, we consider the matching of lattice planes, which could be different in different directions of the film-substrate interface. In the DME framework, the film can have either a fixed or the same orientation relationship with the substrate, depending upon the nature of the misfit. The misfit is accommodated by matching of integral multiples of lattice planes, and there is one extra half-plane (dislocation) corresponding to each domain.

Another important aspect of domain matching epitaxy theory is that it can be used on systems with misfits slightly off perfect one-to-one domain (integral) matching. If the misfit falls in between the perfect matching ratios of planes, then the size of the domain can vary in a systematic way to accommodate the additional misfit. By this theory, additional misfit can be accommodated by changing the domain size within the DME framework.

An important feature of the domain epitaxy concept is that most of the strain is relieved quickly within a couple of monolayers, so that the misfit strain can be engineered and

confined near the interface. This makes it possible for the rest of the film to be grown free of defects and lattice strains.

<table>
<tr><th colspan="5">Epitaxy</th></tr>
<tr><td rowspan="3">Homoepitaxy
Film and substrate are same material.</td><td colspan="4">Heteroepitaxy
Film and substrate are different materials.
$f = 2\times\frac{b-a}{b+a}$</td></tr>
<tr><td>Lattice-Matched</td><td>Coherently Lattice-Mismatched</td><td colspan="2">Incoherently Lattice-Mismatched</td></tr>
<tr><td rowspan="2">Lattice-Matched Epitaxial Heterstructures</td><td rowspan="2">Coherently Strained Lattice – Mismatched Heterosepitaxy (or Strained-Layer Epitaxy)</td><td colspan="2">Relaxed Lattice Mismatched Heteroepitaxy</td></tr>
<tr><td>Relaxed after critical thickness</td><td>Relaxed at interface</td></tr>
<tr><td>$f = 0$</td><td>$f \approx 0$
$a \approx b$</td><td>$f = 2\times\frac{b-a}{b+a}$
$0 \le f \le 1\%$</td><td>$f = 2\times\frac{b-a}{b+a}$
$1\% \le f \le 7\%$</td><td>$f_{lattice match} = 2\times\frac{b-a}{b+a}$
$f_{lattice match} \ge 7\%$
$f_{domain match} = 2\times\frac{mb-na}{mb+na}$</td></tr>
<tr><td>Si on Si epitaxy</td><td>GaAs/Ge
Ge/GaAs</td><td>Ge/Si
Si/Ge</td><td>AlN/sapphire
GaAs/Si
Si/GaAs</td><td>TiN/Si(100)
ZnO/sapphire
AlN/Si(111)</td></tr>
</table>

Table 1. Schematic relationship between different epitaxy catagories.

Usually in thin film growth, the lattice parameters between substrates and films are different. Hence depending on the mismatch, the film can grow onto the substrate either

coherently, called *coherently strained lattice –mismatched heterosepitaxy* (or strained-layer epitaxy) or incoherently called *relaxed lattice mismatched heteroepitaxy* as we discussed in section 1.2.1. But in the second case, *relaxed lattice mismatched heteroepitaxy* has two different categories depending on lattice mismatch. In the first category, the relaxation happens after the critical thickness; second category, the relaxation happens exactly at the interface. Both of the categories are clearly shown in figure 3a and 3b. The second category falls into domain matching epitaxy.

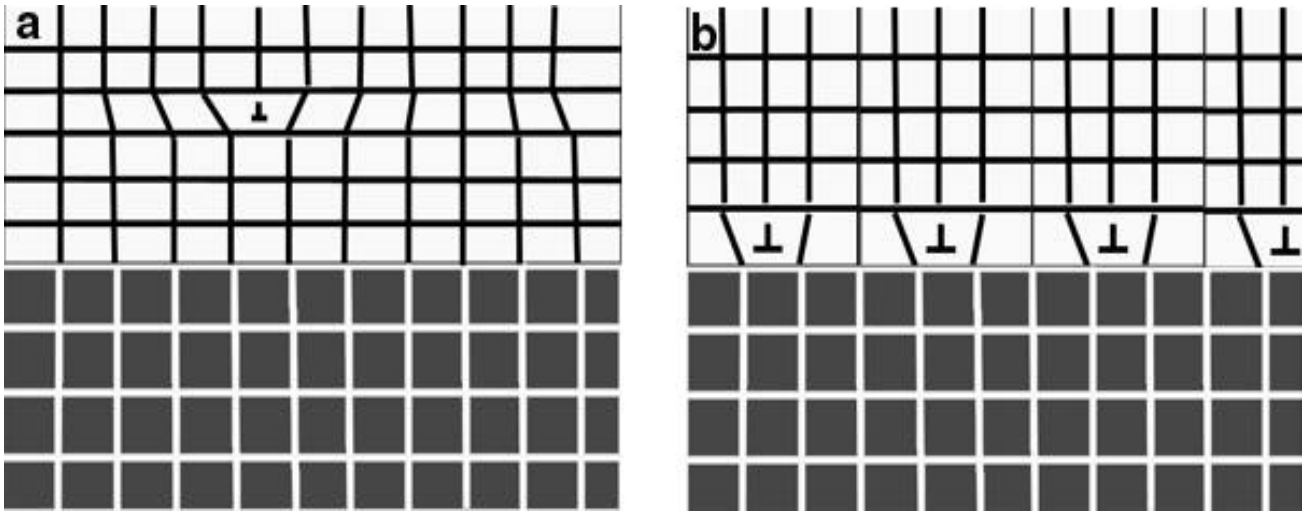

Figure 3. Schematic illustration of two categories of relaxed lattice mismatched heteroepitaxy (a) relaxation happened after critical thickness; (b) relaxation happened at the interface (domain matching epitaxy).

In the strained layer epitaxy, atoms in the film are constrained to the substrate inter-atomic spacing in the plane of interface despite the difference in the film and substrate lattice parameters. Thus significant elastic strain energy is stored in the structure. For

example, accommodation of a lattice mismatch of only 1% in a coherent strained film, produces a stress field about 2 GPa (at shear modulus 5 x 10^{10} Pa, and Poison ratio 0.33) [2]. For a given lattice mismatch the elastic strain energy in the initially coherent film increases linearly with the film thickness. When the strain energy is sufficiently large, at a "critical thickness", the strain at the interface is relieved via the formation of misfit dislocations and this is called relaxed lattice mismatch mechanism of epitaxy. If the critical thickness is not equal to "0", it is the first category: relaxation after critical thickness. If in heterostructures with a very large lattice mismatch (>10%) such as, TiN on Si with lattice misfit 24.6%, the strain in the film is so large at the very initial stages that the film can not grow coherently from the beginning. It is called domain matching epitaxy. In such case the epitaxial growth is achieved via formation of domains when $na_f = (n \pm 1)a_s$, where the a_f and a_s are the film and the substrate lattice parameters, respectively, and n is an integer.[5] The coherency between the film and the substrate is preserved within the domain, while there is a cross-grid of misfit dislocations separating the domains.

After studied various cases of domain matching epitaxy, Narayan and his coworkers presented the master plot of domain matching epitaxy, which includes all the possible configurations of domain matching in nature according to various tensile strain in the heterostructures, see figure 4.

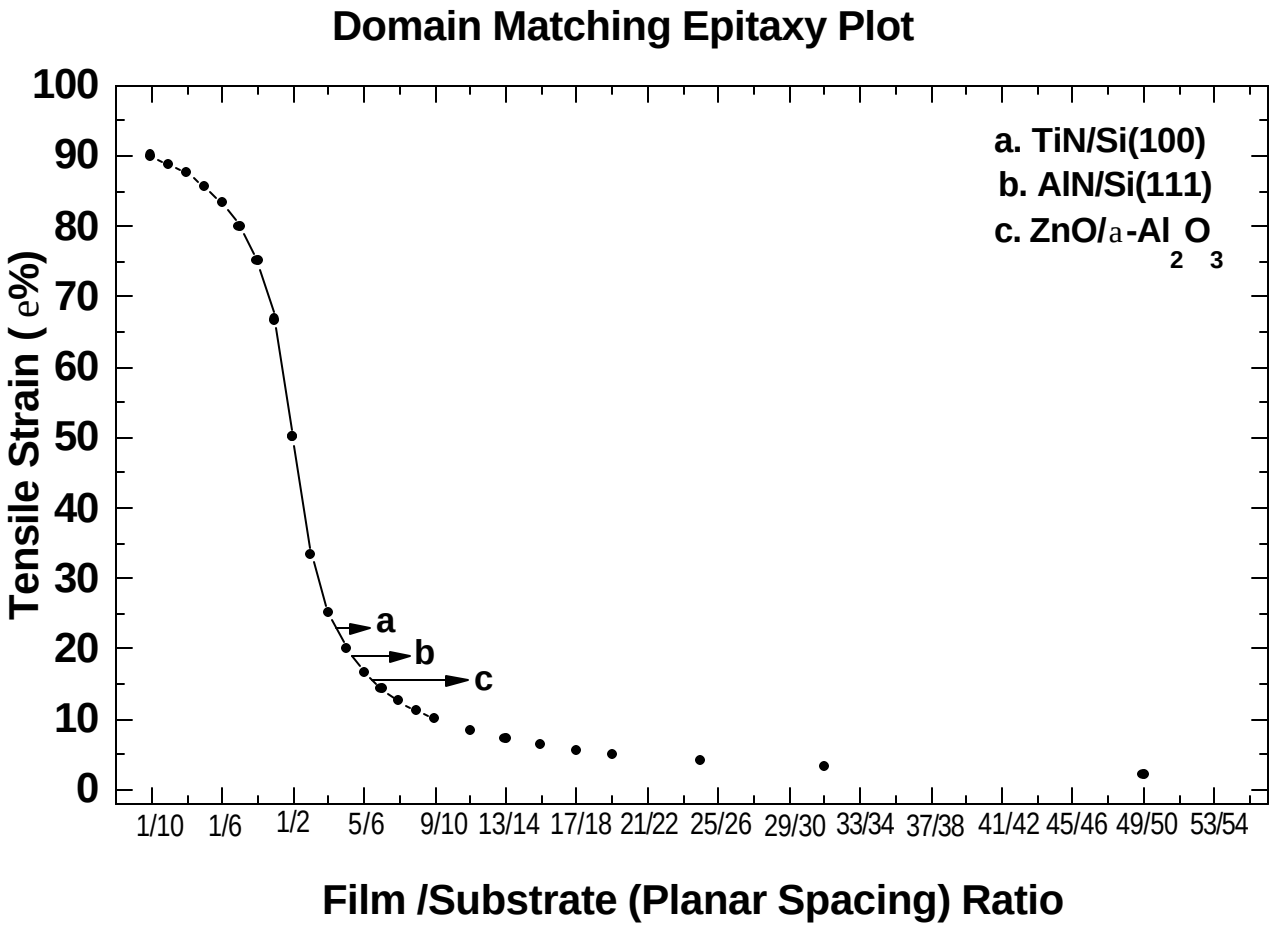

Figure 4. Domain Matching Epitaxy plot of tensile strain vs. possible domain matching ratio.

If any new epitaxy growth system needs to be set up, we can calculate the lattice matching and tensile strain by the lattice parameter of these two materials, then find the possible matching ratio between them from the above plot. If the ratio is exactly fall into one of the integer number ratio, it is quite possible they can grow epitaxially by domain matching epitaxy. If they fall in between two integer number ratio, they will have more

than one domain matching ratio. By varying the domain-size, which is equal to intregral multiple of lattice planes, in a periodic fashion, it is possible to accommodate additional misfit beyond perfect domain matching.

Several examples shown in domain matching epitaxy master plot which have been proved by experimental are simply described in the following:

TiN / Si

Relatively large lattice mismatch f=24.6% and high interfacial energy result in misfit dislocations along the TiN/Si interface, because the strain in the film is so large at the very initial stages that the film can not grow coherently from the beginning. In figure 5, misfit dislocations are clearly visible along the interface of TiN/Si and marked as the extra half planes of dislocation. The short ordering of these misfit dislocations is clearly observed as 3:4 relationship, which means that 4 atomic planes of TiN (111) align with 3 atomic planes of Si(111), according to domain matching epitaxy master plot, in figure 4. And every two set of extra half planes compose one 90^o dislocation as shown in figure 5. These 90^o dislocations are orderly distributed along the interface and burgers vector of these misfit dislocation is identified as $\frac{a}{2}(110)$ lying in {111} planes. [19] The two sets of a/2 <110> dislocations combine at the interface to produce a/2 <110> dislocations lying in the {001} interface. This dislocation reaction can be described as: a/2[101](11-1) + a/2[01-1](111) → a/2[110](001). This is first for a/2<110> dislocation in {111} planes of sodium chloride structure. These new dislocations or slip systems may impact mechanical and physical properties of TiN films or materials of sodium chloride structure.

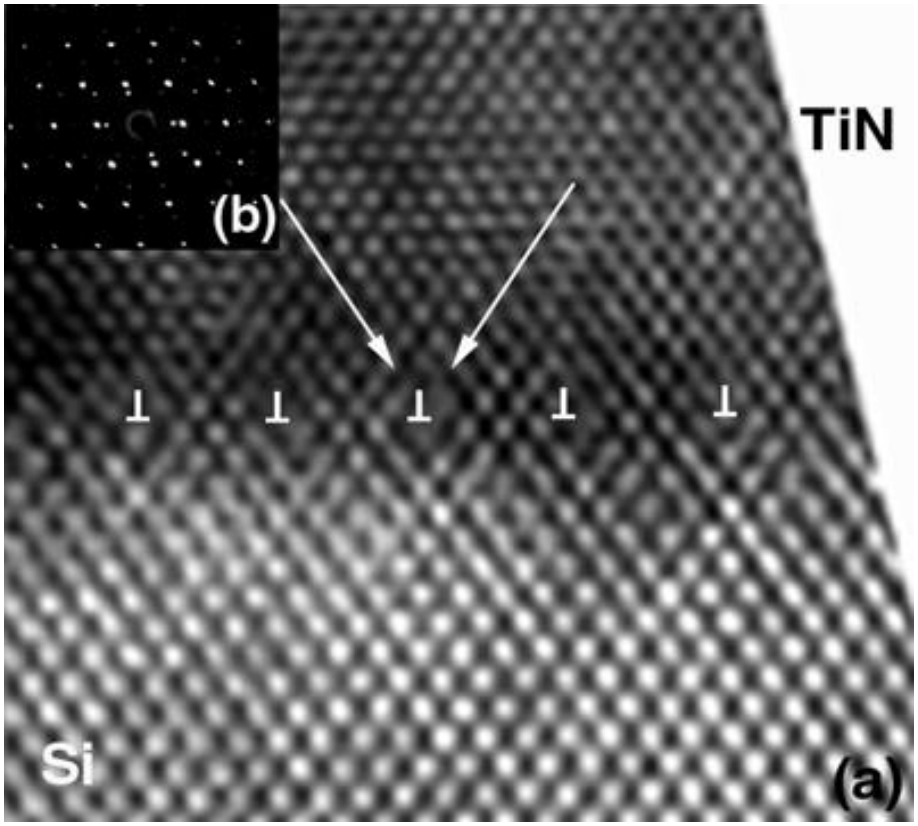

Fig. 5. HRTEM <110> cross-section image (a) and SAD (b) of epitaxial TiN on Si(100). Arrows marked two set set of extra half planes which compose one 90^{o} dislocation. (Ref 19)

AlN/ Si(111)

Epitaxial growth of AlN (0001) with hexagonal wurtzite structure (a=3.11A, c=4.982A) on silicon (111) substrate occurs via matching of four silicon {220} planes with five $\{2\bar{1}\bar{1}0\}$planes of AlN from the master plot. The corresponding diffraction pattern of AlN $<2\bar{1}\bar{1}0>$// Si <110> confirmed the single crystalline AlN with hex-on-cube epitaxial relationship with AlN $[2\bar{1}\bar{1}0]$// Si[110] and AlN $[01\bar{1}0]$ // Si[211]. The spacing of $\{2\bar{1}\bar{1}0\}$AlN planes (a/2=1.556A) result in close to 19% strain with {220} planes of silicon. Using this strain, we found that 5 AlN $\{2\bar{1}\bar{1}0\}$ / 4 Si {220} matching results with less than 1% residual strain. Figure 6 shows a Fast Fourier Transformed image from cross-section HRTEM micrograph. The alignment of $\{2\bar{1}\bar{1}0\}$ planes of AlN with {220} planes of silicon is clearly shown. In this field of view, five planes of AlN clearly match with four planes of silicon with one exception where six planes of AlN match with 5 planes of silicon. This is predicted from the master diagram in fig1. for a 19% strain. Thus the direction from the ideal 5/4 matching corresponding 20% strain are accommodated by variation in domain size, rather than additional set of secondary dislocation to relieve this additional strain.[20]

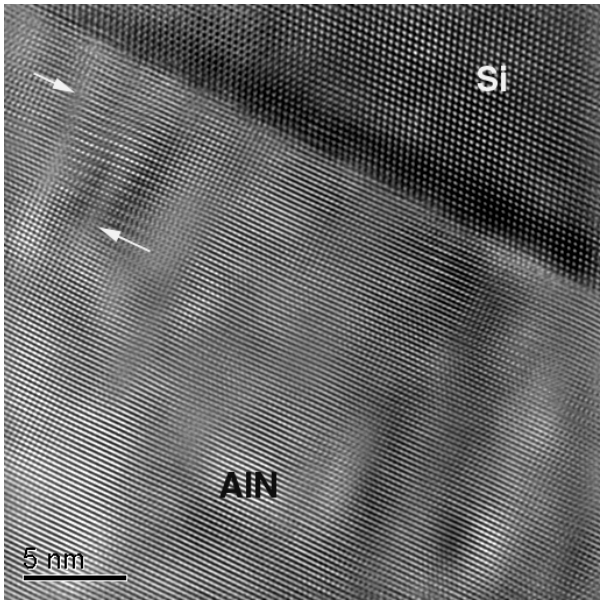

Figure 6. (a) High resolution cross-section TEM image of AlN/Si<110> to show the quality of the film

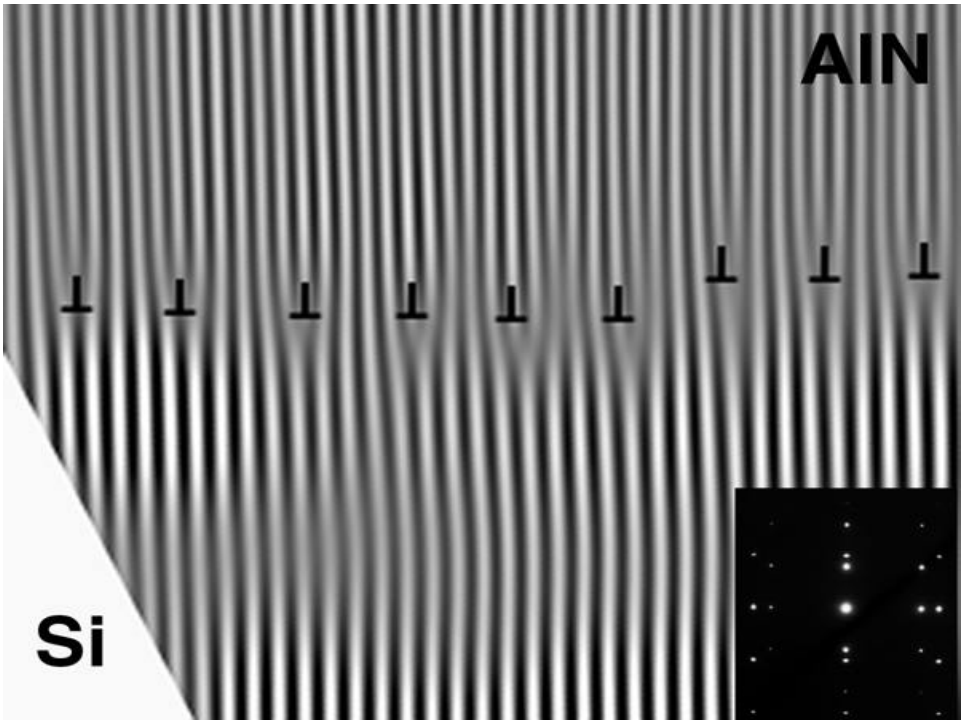

Figure 6. (b) Fast Fourier filtered HRTEM image using opposite AlN $\{2\bar{1}\bar{1}0\}$ / Si {220}reflexes showing the match of the corresponding planes. Misfit dislocations at the

interface are indicated. (AlN/Si<211>) It clarified the 5:4 matching between AlN $\{2\bar{1}\bar{1}0\}$ / Si {220} lattice planes. (Ref. 20)

Domain Epitaxy of ZnO /a-Al_2O_3.

There is a growing interest in growing high quality thin films of its alloys for light emitting diodes(LEDs) and laser diodes (LEDs) applications. The bandgap of ZnO can be tuned by alloying with MgO (8.0 eV, upshift) or with CdO(1.9 eV, downshift) the ZnO can be also as a template for III-nitride growth on sapphire substrate. Therefore, the growth of high quality ZnO thin films on practical substrate (sapphire) has considerable interests. By Pulsed Laser Epitaxy, high quality epitaxial ZnO films were grown on sapphire. The epitaxial relations are ZnO $[01\bar{1}0]$//sapphire $[2\bar{1}\bar{1}0]$ and ZnO (0001)// sapphire (0001). This inplane orientation relation corresponds to a 30^o rotation of ZnO basal planes with respect to sapphire substrate, which is similar to the epitaxial growth characteristics of AlN and GaN on sapphire. Under these conditions, approximately 18% of the lattice mismatch across the interface is accommodated via domain matching epitaxy where 6 units of the film match with 7 of the substrate, which is shown in figure 8(b).

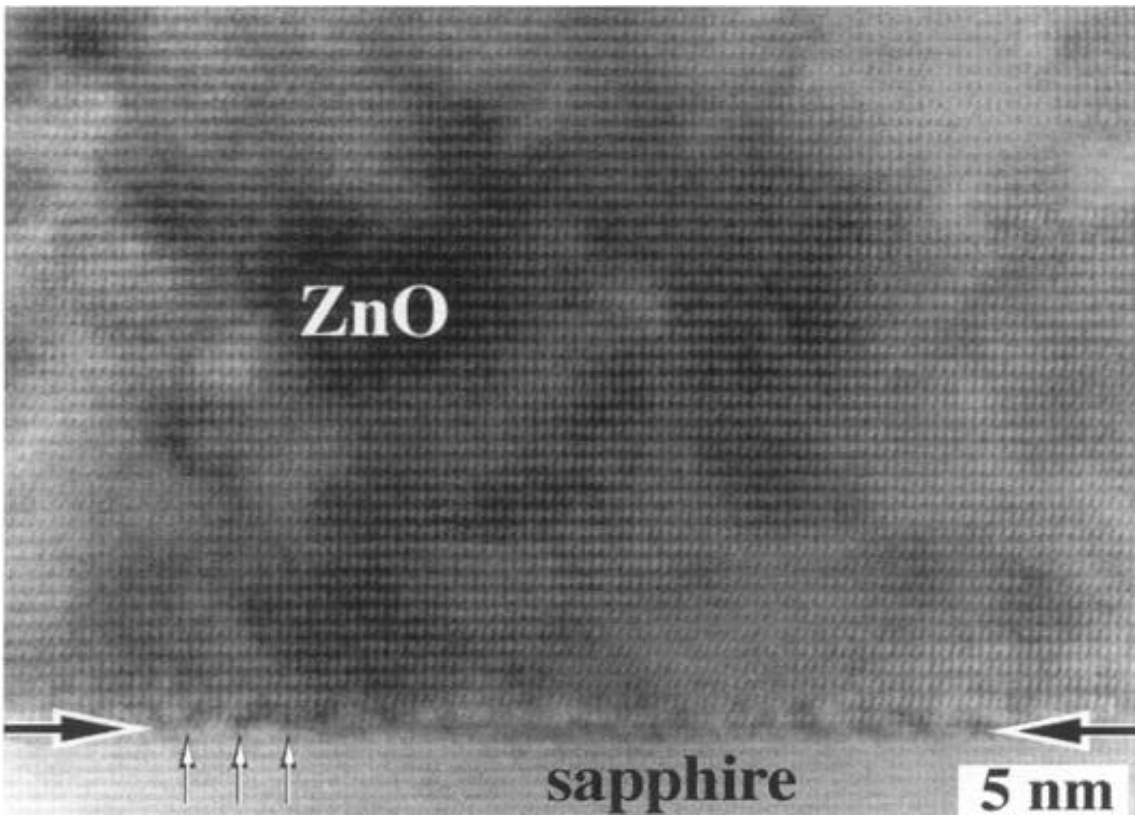

Figure 7. (a) High resolution TEM cross-sectional image of the ZnO film near the film/substrate interface (shown by black arrows). The terminating planes corresponding to the misfit dislocations are indicated by white arrows. (Ref. 21)

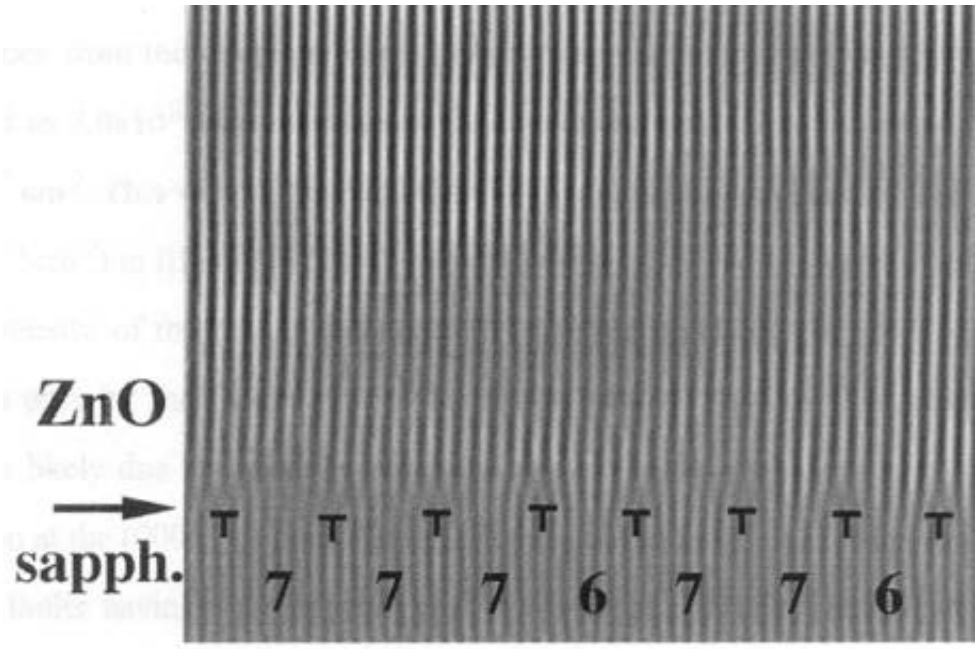

Figure 7 (b) Fourier filtered image using opposite ZnO $\{01\bar{1}0\}$//sapphire $\{2\bar{1}\bar{1}0\}$ reflexes showing the match of the corresponding planes. Misfit dislocations at the interface are indicated. Numbers in the bottom of the picture correspond to the number of planes between the misfit dislocations. Note that every 7^{th} or 6^{th} $\{2\bar{1}\bar{1}0\}$plane of sapphire terminates at the interface. (Ref 21)

From Above discussion, one can conclude that, according to domain matching epitaxy, the possibility for high lattice mismatch system to grow epitaxially increased. More and more new material systems which have large lattice mismatch could be realized by domain matching theory and further benefit the development of new structures and

devices. By matching integral multiples of major planes between the film and the substrate, it is possible to grow films with small as well as large misfits. The systematic variations in domain sizes are created to accommodate misfits that fall between the integral multiples. As the domain size changes, the nature of the dislocations remains the same. For large misfit strains, the critical thickness is less than one to two monolayers, so dislocations corresponding to full lattice relaxation are generated at or within a monolayer of the interface; and the remainder of the film can be grown virtually strain and misfit-dislocation free. Thus, the DME concept can be used to engineer and confine misfit strains near the interface, and films with larger misfits can be grown with a fewer number of defects in the active regions, compared to the films with smaller misfits grown by LME. The nature of misfit dislocations in terms of Burgers vectors and habit planes are determined by geometrical constraints, rather than by deformation in the normal slip systems. This is similar to the observations of unusual dislocation structures at the grain boundaries formed as a result of geometrical constraints. The formation of a/2 <100> dislocations in {111} planes in TiN has been shown to be a result of geometrical constraints during domain epitaxy on Si(100) substrate. Thus, domain epitaxy provides a mechanism to grow epitaxial films on substrates with large misfits, and opens a new frontier in next-generation solid state technology.

References

1. M.Ohring, *The Materials Science of Thin Films,* Academic Press, Inc., 1992.

2. R. Hull and J.C. Bean, Principles and Concepts of Strained-Layer Epitaxy, Ed. T. Pearsal, *Strained-Layer Superlattices: Materials Science and Technology*, 1991.

3. J. Singh, *Physics of Semiconductors and Their Heterostructures*, McGraw-Hill, Inc., 1993.

4. L. Eckertova, *Physics of Thin Films*, Plenum Press, 1986.

5. J. Narayan, P. Tiwari, X. Chen, J. Singh, R. Chowdhury and T. Zheleva, *Appl. Phys. Lett.* **61**, 1290(1992). (J Narayan, U.S. Patent#5, 406,123, April 11,1995)

6. J. Woltersdorf, *Appl. Surf. Sci*., **11**, 495, (1982).

7. P. S. Peercy, *J. Mater. Res.*, **5**, 4, (1990).

8. E. Bauer, *Appl. Surf. Sci*. **11**, 479(1982).

9. F. C. Frank and J. H. van der Merve, *Proc. Roy. Soc*., **A198**, 205 (1949).

10. J. H. van der Merve, *J. Appl. Phys.*, **34**, 123(1962).

11. J. W. Matthews and A. E. Blackslee, J. Cryst. Growth, 27, 118(1974)

12. J. W. Matthews, J. VAc. Sci. Technol. 12, 126(1975)

13. M. Ichimura, and J. Narayan, Phi. Mag. (1995).

14. J. Narayan and S. Sharan, *Mater. Sci. Eng*., **B.10**, 261(1991).

15. S. A. Dregia and J. P. Hirth, *J. Appl. Phys.*, **69**, 2169(1991).

16. D. J. Eaglesham, E. P. Kvam, D. M. Maher, C. J. Humphreys, and J. C. Ban, Phil. Mag. A59, 1059 (1089).

17. S. Oktyabrsky, H. Wu, R. D. Vispute, and J. Narayan, Phil. Mag., A71, 3, 537(1990).

18. A. Nabdedkar and J. Narayan, Phil. Mag. A61, (6), 873(1990)

19. H. Wang, A. Tiwari, A. Kvit, X. Zhang and J. Narayan, *Appl. Phys. Lett*., **80**, No 13, 3223, (2002).

20. H. Wang, T. Rawdanowicz, X. Zhang, J. Narayan, Submitted to Appl. Phys. Lett. 2002.

21. K. Dovidenko, S. Oktyabrisky, J. Narayan and Razeghi, J. Appl. Phys., **79**, 2439, 1996.